

Spatial Wilson Loops and Energy Loss for Heavy Quarks in Magnetized HQCD Model

Irina Ya. Aref'eva^a, Ali Hajilou^{a,b}, Kristina Rannu^c and Pavel Slepov^a

^a*Steklov Mathematical Institute, Russian Academy of Sciences,
Gubkina str. 8, 119991, Moscow, Russia*

^b*School of Particles and Accelerators, Institute for Research in Fundamental
Sciences (IPM), P.O. Box 19395-5531, Tehran, Iran*

^c*Peoples Friendship University of Russia,
Miklukho-Maklaya str. 6, 117198, Moscow, Russia*

E-mail: arefeva@mi-ras.ru, hajilou@mi-ras.ru, rannu-ka@rudn.ru,
slepov@mi-ras.ru

ABSTRACT: We investigate the effective potential and the string tension for the spatial Wilson loop (SWL) in hot dense QGP with two types of anisotropy, i.e. external magnetic field and spatial anisotropy, employing a holographic approach for the heavy quark model. In this approach, the string is extended in the 5th, holographic direction and has a turning point either on a dynamical wall (DW) configuration or on the horizon configuration in the 5th direction. We obtain the magnetic catalysis behavior for a phase transition between DW and horizon configuration of the string. The structure of the phase diagram does not depend on the boundary conditions choice for the dilaton field. Inclusion of the external magnetic field and spatial anisotropy enhance the string tension in the horizon configuration, namely drag force. For the spatially isotropic case $\nu = 1$ at different magnetic field values the string tension is proportional to T^2 and is qualitatively consistent with lattice results. However, for the anisotropic case, $\nu = 4.5$, it deviates from the quadratic term.

KEYWORDS: holography, AdS/QCD, spatial Wilson loops, heavy quarks, magnetic catalysis, string tension

Contents

1	Introduction	2
2	Holographic set up for heavy quarks	4
2.1	Background	4
2.2	Thermodynamics	5
3	Wilson loops and effective potential	8
3.1	Born-Infeld type action	8
3.2	Dynamical wall equations	8
4	Numerical results	11
4.1	Spatial Wilson loop \mathcal{W}_{xY_1}	11
4.1.1	Zero-boundary condition	11
4.1.2	Physical-boundary condition	15
4.2	Spatial Wilson loop \mathcal{W}_{xY_2}	19
4.3	Spatial Wilson loop $\mathcal{W}_{y_1Y_2}$	23
4.4	Phase diagrams in particular SWL orientations	27
5	Comparing the spatial string tension with lattice calculations	29
6	Conclusion	33
A	Solution of EOMs	37
B	Arbitrary orientations of Wilson loop	38
C	String tension at DW and horizon configurations	41

1 Introduction

The holographic approach is a non-perturbative method for investigating the strongly coupled regime of quantum chromodynamics (QCD). There are two different classes of holographic models: “top-down” and “bottom-up”. Holographic QCD is a suitable candidate for studying the quark-gluon plasma (QGP) observed in ultrarelativistic heavy-ion collisions (HIC) [1–6]. In particular, the phase diagram of QCD has received a lot of attention to study. In the “bottom-up” holographic approach the choice of the metric warp factor has a crucial influence on the phase transition structure of QCD [7–18]. This choice is different for the light- and heavy-quark models and should correspond to the lattice results known as the Columbia plot [19, 20]. In [21–34] different isotropic and anisotropic models were proposed to study QCD using holography.

Taking into account the anisotropy in the holographic model [35–46] is important because of QGP, which is spatially anisotropic after HIC. The first Maxwell field in the model supports the chemical potential in the boundary theory. In addition, to consider two types of anisotropy due to the external magnetic field and spatial anisotropy, two Maxwell fields need to be introduced into the model [45]. The model that we use in this research was developed in [45] with modified warp-factor. It produces the direct magnetic catalysis phenomenon for heavy quarks that is expected from lattice calculations. The Wilson loops calculations for the heavy-quarks model with a more simple warp-factor [47] was done in [48]. The second and third Maxwell fields support the magnetic field and the spatial anisotropy defined by ν in the boundary theory, respectively. An anisotropic model with $\nu = 4.5$ [49] has been shown to be able to reproduce the energy dependence of the total multiplicity of particles created in HIC [50]. For the light-quark model one can see [18] and for the heavy-quark model [14].

The experiments in the relativistic HIC have addressed the possibility of new parameters in the QCD phase diagram. A strong magnetic field $eB \sim 0.3 \text{ GeV}^2$ is created in the early stages of non-central HIC [51–53]. Therefore, an external magnetic field can be considered the second anisotropy affecting the characteristics of QCD. Magnetized QCD has received a lot of attention in recent years. In particular, recently the magnetic field effect on the running coupling of QCD was investigated in [54–56]. Holographic models [47, 57–63] studied the effect of magnetic field on the different properties of QCD.

Temporal Wilson loops and SWLs in the holographic approach have been used to study different properties of QCD [39, 64, 65]. Temporal Wilson loops are used to investigate the confinement/deconfinement phase transition in QCD. The drag

force acting on the heavy quark, moving in QGP, comes from its interaction with the plasma, that was investigated in holographic QCD models [66–68]. For isotropic models the SWL string tension is proportional to the corresponding drag force [69, 70]. For anisotropic models this relation takes place with a small modification, see [6]. Therefore, one can calculate SWL to investigate the drag forces for a heavy quark moving in QGP. The drag forces defining energy loss are studied intensively in holographic models [71–76].

In this research we consider the Einstein-three-Maxwell-dilaton action, set up in [45], to investigate the effective potential, string tension and to compare our results on the string tension with the drag force and lattice calculations. This model possesses two types of anisotropy, i.e. spatial anisotropy and external magnetic field. We study the effect of these anisotropies on the phase transition temperature obtained by Wilson loops. To do so, we considered SWL in three different orientations, i.e. \mathcal{W}_{xY_1} , \mathcal{W}_{xY_2} , and $\mathcal{W}_{y_1Y_2}$, referred to as the first, second, and third orientations, respectively.

This paper is organized as follows. In Sect. 2 we introduce a fully anisotropic 5-dimensional holographic set up for heavy quarks model. Sect. 3 presents the Born-Infeld action to get the DW equations. In Sect. 4 we obtain numerical results for particular SWL orientations. Sect. 5 investigates the connection between the string tension and the drag force and compares it with lattice results. In Sect. 6 we summarize our results. The paper is complemented by an appendix A, which describes the explicit forms of the equations of motion (EOMs). In appendix B arbitrary orientations of the Wilson loop are studied, and in appendix C the string tension at the DW and horizon configurations are derived.

2 Holographic set up for heavy quarks

In this section we consider the background with two types of anisotropy, i.e. spatial anisotropy and external magnetic field, that are found in [45], and the thermodynamical properties of this model.

2.1 Background

We consider the Lagrangian with three Maxwell fields in Einstein frame, used in [45]:

$$\mathcal{L} = \sqrt{-\mathfrak{g}} \left[R - \frac{f_0(\phi)}{4} F_0^2 - \frac{f_1(\phi)}{4} F_1^2 - \frac{f_3(\phi)}{4} F_3^2 - \frac{1}{2} \partial_\mu \phi \partial^\mu \phi - V(\phi) \right], \quad (2.1)$$

where \mathfrak{g} is the determinant of the metric tensor, R is Ricci scalar, ϕ is the dilaton field, $V(\phi)$ is the dilaton field potential, and $f_0(\phi)$, $f_1(\phi)$ and $f_3(\phi)$ are the coupling functions associated with stresses F_0 , F_1 and F_3 of Maxwell fields, respectively. The electromagnetic tensor is defined as $F_{\rho\sigma} = \partial_\rho A_\sigma - \partial_\sigma A_\rho$ and the indexes ρ and σ numerate the spacetime coordinates (t, x_1, x_2, x_3, z) , with z being the radial holographic coordinate. Maxwell fields F_0 , F_1 and F_3 are considered the first, the second, and the third, respectively.

We take the following ansatz for the metric [45], that in the Einstein frame is

$$ds^2 = \frac{L^2}{z^2} \mathfrak{b}(z) \left[-g(z) dt^2 + dx^2 + \left(\frac{z}{L} \right)^{2-\frac{2}{\nu}} dy_1^2 + e^{c_B z^2} \left(\frac{z}{L} \right)^{2-\frac{2}{\nu}} dy_2^2 + \frac{dz^2}{g(z)} \right], \quad (2.2)$$

$$\mathfrak{b}(z) = e^{2\mathcal{A}(z)}, \quad (2.3)$$

and for the matter fields:

$$\phi = \phi(z), \quad (2.4)$$

$$\begin{aligned} F_0 - \text{electric anzats} \quad & A_0 = A_t(z), \quad A_i = 0, \quad i = 1, 2, 3, 4, \\ F_k - \text{magnetic ansatz} \quad & F_1 = q_1 dy^1 \wedge dy^2, \quad F_3 = q_3 dx \wedge dy^1, \end{aligned} \quad (2.5)$$

where L is the AdS-radius, $\mathfrak{b}(z)$ is the warp factor in Einstein frame, that is specified by a scale factor $\mathcal{A}(z)$, $g(z)$ is the blackening function, and ν is the parameter of primary anisotropy created by the non-symmetry of HIC, such that $\nu = 1$ corresponds to spatially isotropic background and choice $\nu = 4.5$ for anisotropic background is in agreement with the experimental data on the energy dependence of the total multiplicity of particles produced in HIC [50]. The coefficient of secondary anisotropy c_B is related to the external magnetic field F_3 . Different choices of $\mathcal{A}(z)$ determine the description of the model with heavy/light quarks. For heavy quarks we considered $\mathcal{A}(z) = -cz^2/4$ [14, 16, 47] and for light quarks $\mathcal{A}(z) = -a \ln(bz^2 + 1)$ [18]. In this research our choice of $\mathcal{A}(z)$ for the heavy quarks model is [45]

$$\mathcal{A}(z) = -cz^2/4 - (p - c_B q_3)z^4, \quad (2.6)$$

where $c = 4R_{gg}/3$, $R_{gg} = 1.16$ GeV 2 , $c = 1.547$ GeV 2 , and $p = 0.273$ GeV 4 are parameters, that can be fixed with lattice and experimental data for zero magnetic field, i.e. for $c_B = 0$ case [10].

Varying the Lagrangian (2.1) by using the ansatz (2.2)-(2.5) leads to the EOMs for Einstein, dilaton and Maxwell fields, that can be found in appendix A (see equations (A.5)-(A.10)). The EOMs are solved with the boundary conditions

$$A_t(0) = \mu, \quad A_t(z_h) = 0, \quad (2.7)$$

$$g(0) = 1, \quad g(z_h) = 0. \quad (2.8)$$

For the dilaton field, different boundary conditions can be used. We denoted the boundary condition for $\phi(z, z_0)$, so that

$$\phi(z, z_0) \Big|_{z=z_0} = 0. \quad (2.9)$$

We consider two types of boundary conditions by taking different z_0 [18, 77–80]. The zero-boundary condition is chosen as

$$z_0 = \epsilon, \quad (2.10)$$

where $0 < \epsilon \ll 1$, and another boundary condition is

$$z_0 = \mathfrak{z}(z_h), \quad (2.11)$$

where $\mathfrak{z}(z_h)$ is a smooth function of z_h , different for light and heavy quarks. For heavy quarks, we take

$$z_0 = \mathfrak{z}(z_h) = e^{(-\frac{z_h}{4})} + 0.1, \quad (2.12)$$

known as a physical-boundary condition, for more details, see [18, 77–80]. We note that in this paper we considered the zero-boundary conditions, i.e. (2.10) in our calculations, and the physical-boundary condition (2.12) has just been used in subsection 4.1.2.

2.2 Thermodynamics

To investigate thermodynamics we use the following formulas for temperature and entropy

$$T = \frac{\sqrt{g_{tt'} g^{zz'}}}{4\pi} \Big|_{z=z_h} = \frac{\sqrt{g_{00'} g^{44'}}}{4\pi} \Big|_{z=z_h} = \frac{|g'(z)|}{4\pi} \Big|_{z=z_h}, \quad (2.13)$$

$$s = \frac{\sqrt{g_{xx} g_{y_1 y_1} g_{y_2 y_2}}}{4G_5} \Big|_{z=z_h} = \frac{\sqrt{g_{11} g_{22} g_{33}}}{4G_5} \Big|_{z=z_h}, \quad (2.14)$$

where G_5 is the gravitational constant that in our calculations we set $8\pi G_5 = 1$ and $g(z)$ is the blackening function given by

$$g(z) = e^{c_B z^2} \left[1 - \frac{\tilde{I}_1(z)}{\tilde{I}_1(z_h)} + \frac{\mu^2 (2R_{gg} + c_B(q_3 - 1)) \tilde{I}_2(z)}{L^2 \left(1 - e^{(2R_{gg} + c_B(q_3 - 1)) \frac{z_h^2}{2}} \right)^2} \left(1 - \frac{\tilde{I}_1(z)}{\tilde{I}_1(z_h)} \frac{\tilde{I}_2(z_h)}{\tilde{I}_2(z)} \right) \right], \quad (2.15)$$

$$\tilde{I}_1(z) = \int_0^z e^{(2R_{gg} - 3c_B) \frac{\xi^2}{2} + 3(p - c_B q_3) \xi^4} \xi^{1+\frac{2}{\nu}} d\xi, \quad (2.16)$$

$$\tilde{I}_2(z) = \int_0^z e^{(2R_{gg} + c_B(\frac{q_3}{2} - 2)) \xi^2 + 3(p - c_B q_3) \xi^4} \xi^{1+\frac{2}{\nu}} d\xi. \quad (2.17)$$

Using the metric (2.4) and the scale factor (2.6) with equations (2.13) and (2.14) one can obtain the temperature and entropy:

$$T = \left| - \frac{e^{(2R_{gg} - c_B) \frac{z_h^2}{2} + 3(p - c_B q_3) z_h^4} z_h^{1+\frac{2}{\nu}}}{4\pi \tilde{I}_1(z_h)} \times \right. \\ \left. \times \left[1 - \frac{\mu^2 (2R_{gg} + c_B(q_3 - 1)) \left(e^{(2R_{gg} + c_B(q_3 - 1)) \frac{z_h^2}{2}} \tilde{I}_1(z_h) - \tilde{I}_2(z_h) \right)}{L^2 \left(1 - e^{(2R_{gg} + c_B(q_3 - 1)) \frac{z_h^2}{2}} \right)^2} \right] \right|, \quad (2.18)$$

$$s = \frac{1}{4G_5} \left(\frac{L}{z_h} \right)^{1+\frac{2}{\nu}} e^{-(2R_{gg} - c_B) \frac{z_h^2}{2} - 3(p - c_B q_3) z_h^4}.$$

In Fig. 1 the temperature as a function of horizon $T(z_h)$ for different μ at fixed $\nu = 1$ (A), $\nu = 4.5$ (B), and different ν and c_B at fixed $\mu = 0$ (C), $\mu = 0.2$ GeV (D) is plotted. Figs. 1A and 1B show, that the temperature of the Hawking-Page like phase transition T_{HP} is lower for larger μ in both isotropic and anisotropic cases. Figs. 1C and 1D show, that primary anisotropy ν decreases T_{HP} for both zero and non-zero values of chemical potential.

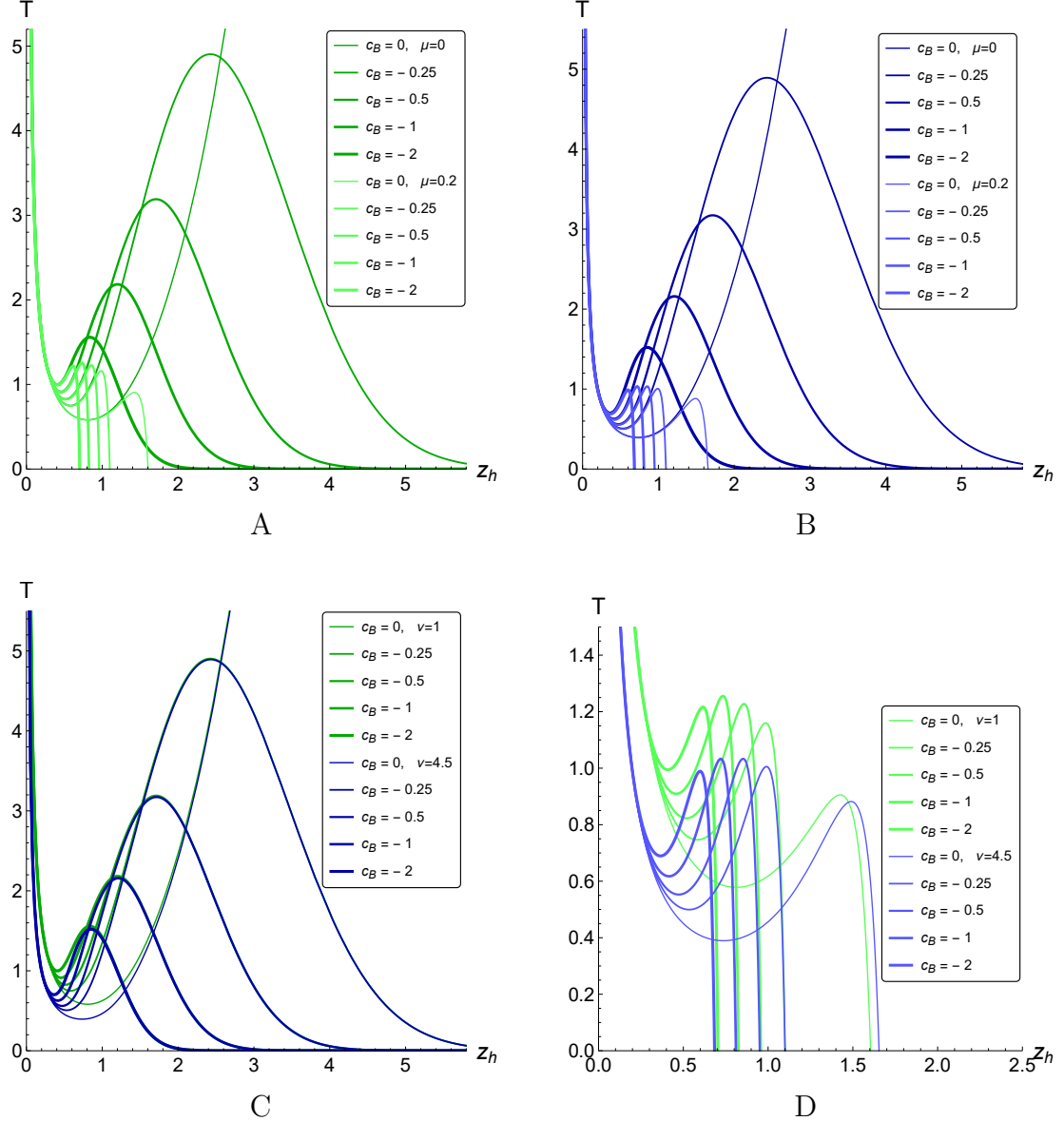


Figure 1. Temperature as a function of horizon $T(z_h)$ for (A) different μ at fixed $\nu = 1$, (B) $\nu = 4.5$, and (C) different ν and c_B at fixed $\mu = 0$, (D) $\mu = 0.2$ GeV; $q_3 = 5$, $R_{gg} = 1.16$ GeV 2 , $p = 0.273$ GeV 4 ; $[T] = [\mu] = [z_h]^{-1} = [c_B]^{\frac{1}{2}} = \text{GeV}$.

3 Wilson loops and effective potential

3.1 Born-Infeld type action

The actions that are considered for SWL, temporal Wilson loop, light-like Wilson loop and holographic entanglement entropy [4, 16, 48, 81–83] are the specific cases of the Born-Infeld action

$$\mathcal{S} = \int_{-\ell/2}^{\ell/2} M(z(\xi)) \sqrt{\mathcal{F}(z(\xi)) + (z'(\xi))^2} d\xi, \quad (3.1)$$

where ℓ is the interquark distance, ξ denotes the “time”, and $\mathcal{F}(z)$ is an arbitrary function. The action (3.1) describes the dynamical system with a dynamic variable $z = z(\xi)$. The associated effective potential is

$$\mathcal{V}(z(\xi)) \equiv M(z(\xi)) \sqrt{\mathcal{F}(z(\xi))}. \quad (3.2)$$

After some algebra (for more detail see appendix C) one can obtain the action \mathcal{S} and the length ℓ for DW and horizon configurations. The string tension can be obtained for two different configurations:

- the DW configuration

$$\sigma_{DW} = M(z_{DW}) \sqrt{\mathcal{F}(z_{DW})}, \quad (3.3)$$

- the horizon configuration

$$\sigma_{z_h} = \mathfrak{m}(z_h) \sqrt{\mathfrak{F}(z_h)}, \quad (3.4)$$

where σ_{DW} and σ_{z_h} are the spatial string tension in the DW and horizon configurations. We will investigate the temperature dependence of the string tension for two configurations and three WL orientations in Sect. 4.

3.2 Dynamical wall equations

Obtaining general results for spatial Wilson loops and effective potential, we consider a fully anisotropic background

$$ds^2 = G_{\mu\nu} dx^\mu dx^\nu = \frac{L^2 \mathfrak{b}_s(z)}{z^2} \left[-g(z) dt^2 + \mathfrak{g}_1 dx^2 + \mathfrak{g}_2 dy_1^2 + \mathfrak{g}_3 dy_2^2 + \frac{dz^2}{g(z)} \right] \quad (3.5)$$

and use it to calculate SWLs for different orientations. Here $\mathfrak{b}_s(z) = \mathfrak{b}(z) e^{\sqrt{\frac{2}{3}}\phi(z)}$ is the warp factor in the string frame, and $\mathfrak{g}_1, \mathfrak{g}_2, \mathfrak{g}_3$ are anisotropic functions depending on z .

To get the DW equations, let us take the special cases of (B.12) and (B.13), considering the particular orientations of the SWLs.

- The first orientation (xY_1 -plane): $\phi = 0, \theta = 0, \psi = 0$;
 $a_{11} = a_{22} = a_{33} = 1, a_{12} = a_{21} = a_{31} = a_{31} = a_{32} = a_{23} = 0$:

$$\mathcal{S}_{xY_1} = \frac{1}{2\pi\alpha'} \int_{\mathcal{P}} \left(\frac{L^2 \mathfrak{b}_s}{z^2} \right) \sqrt{\left(\mathfrak{g}_1 \mathfrak{g}_2 + \frac{z'^2}{g} \mathfrak{g}_2 \right)} d\xi^1 d\xi^2, \quad (3.6)$$

$$\mathcal{V}_1 \equiv \mathcal{V}_{xY_1}(z(\xi)) = \frac{1}{2\pi\alpha'} \left(\frac{L^2 \mathfrak{b}_s}{z^2} \right) \sqrt{\mathfrak{g}_1 \mathfrak{g}_2}. \quad (3.7)$$

- The first orientation (Xy_1 -plane)¹: $\phi = \pi/2, \theta = 0, \psi = 0$;
 $a_{21} = a_{33} = -a_{12} = 1, a_{11} = a_{13} = a_{22} = a_{23} = a_{31} = a_{32} = 0$:

$$\mathcal{S}_{Xy_1} = \frac{1}{2\pi\alpha'} \int_{\mathcal{P}} \left(\frac{L^2 \mathfrak{b}_s}{z^2} \right) \sqrt{\left(\mathfrak{g}_1 \mathfrak{g}_2 + \frac{z'^2}{g} \mathfrak{g}_1 \right)} d\xi^1 d\xi^2, \quad (3.8)$$

$$\mathcal{V}_1 \equiv \mathcal{V}_{Xy_1}(z(\xi)) = \frac{1}{2\pi\alpha'} \left(\frac{L^2 \mathfrak{b}_s}{z^2} \right) \sqrt{\mathfrak{g}_1 \mathfrak{g}_2}. \quad (3.9)$$

- The second orientation (xY_2 -plane): $\phi = 0, \theta = \pi/2, \psi = 0$;
 $a_{11} = -a_{23} = a_{32} = 1, a_{12} = a_{13} = a_{21} = a_{22} = a_{31} = a_{33} = 0$:

$$\mathcal{S}_{xY_2} = \frac{1}{2\pi\alpha'} \int_{\mathcal{P}} \left(\frac{L^2 \mathfrak{b}_s}{z^2} \right) \sqrt{\left(\mathfrak{g}_1 \mathfrak{g}_3 + \frac{z'^2}{g} \mathfrak{g}_3 \right)} d\xi^1 d\xi^2, \quad (3.10)$$

$$\mathcal{V}_2 \equiv \mathcal{V}_{xY_2}(z(\xi)) = \frac{1}{2\pi\alpha'} \left(\frac{L^2 \mathfrak{b}_s}{z^2} \right) \sqrt{\mathfrak{g}_1 \mathfrak{g}_3}. \quad (3.11)$$

- The third orientation (y_1Y_2 -plane): $\phi = \pi/2, \theta = \pi/2, \psi = -\pi/2$;
 $a_{22} = a_{31} = -a_{13} = 1, a_{11} = a_{12} = a_{21} = a_{23} = a_{32} = a_{33} = 0$:

$$\mathcal{S}_{y_1Y_2} = \frac{1}{2\pi\alpha'} \int_{\mathcal{P}} \left(\frac{L^2 \mathfrak{b}_s}{z^2} \right) \sqrt{\left(\mathfrak{g}_2 \mathfrak{g}_3 + \frac{z'^2}{g} \mathfrak{g}_2 \right)} d\xi^1 d\xi^2, \quad (3.12)$$

$$\mathcal{V}_3 \equiv \mathcal{V}_{y_1Y_2}(z(\xi)) = \frac{1}{2\pi\alpha'} \left(\frac{L^2 \mathfrak{b}_s}{z^2} \right) \sqrt{\mathfrak{g}_2 \mathfrak{g}_3}. \quad (3.13)$$

Note, that the capital letters Y_1, X, Y_2 in the WL orientations indicate the direction the loop contour has an infinite length along.

¹The Nambu-Goto action for Xy_1 -plane coincides with Nambu-Goto action for xY_1 -plane.

The general form of the DW equation, if DW exists, is given by $\mathcal{V}'(z) = 0$ [5, 84]. DW coordinates z_{DW} for SWL in particular orientations are given by

$$\mathcal{D}\mathcal{W}_{xY_1} = \mathcal{D}\mathcal{W}_{Xy_1} \equiv \frac{2\mathfrak{b}'_s(z)}{\mathfrak{b}_s(z)} + \frac{\mathfrak{g}'_1(z)}{\mathfrak{g}_1(z)} + \frac{\mathfrak{g}'_2(z)}{\mathfrak{g}_2(z)} - \frac{4}{z} \Big|_{z=z_{DW}} = 0, \quad (3.14)$$

$$\mathcal{D}\mathcal{W}_{xY_2} \equiv \frac{2\mathfrak{b}'_s(z)}{\mathfrak{b}_s(z)} + \frac{\mathfrak{g}'_1(z)}{\mathfrak{g}_1(z)} + \frac{\mathfrak{g}'_3(z)}{\mathfrak{g}_3(z)} - \frac{4}{z} \Big|_{z=z_{DW}} = 0, \quad (3.15)$$

$$\mathcal{D}\mathcal{W}_{y_1Y_2} \equiv \frac{2\mathfrak{b}'_s(z)}{\mathfrak{b}_s(z)} + \frac{\mathfrak{g}'_2(z)}{\mathfrak{g}_2(z)} + \frac{\mathfrak{g}'_3(z)}{\mathfrak{g}_3(z)} - \frac{4}{z} \Big|_{z=z_{DW}} = 0. \quad (3.16)$$

From the metric (2.2)

$$\mathfrak{g}_1(z) = 1, \quad \mathfrak{g}_2(z) = (z/L)^{2-2/\nu}, \quad \mathfrak{g}_3(z) = (z/L)^{2-2/\nu} e^{c_B z^2}. \quad (3.17)$$

In this case spatial string tensions for three particular orientations, i.e. xY_1 , xY_2 , and y_1Y_2 , are given by

$$\sigma_1 \equiv \sigma_{xY_1} = \frac{1}{2\pi\alpha'} \left(\frac{L^2 \mathfrak{b}_s(z)}{z^2} \right) \sqrt{\mathfrak{g}_1 \mathfrak{g}_2} = \frac{1}{2\pi\alpha'} \left(\frac{L^{1+1/\nu} \mathfrak{b}_s(z)}{z^{1+1/\nu}} \right), \quad (3.18)$$

$$\sigma_2 \equiv \sigma_{xY_2} = \frac{1}{2\pi\alpha'} \left(\frac{L^2 \mathfrak{b}_s(z)}{z^2} \right) \sqrt{\mathfrak{g}_1 \mathfrak{g}_3} = \frac{1}{2\pi\alpha'} \left(\frac{L^{1+1/\nu} \mathfrak{b}_s(z)}{z^{1+1/\nu}} \right) e^{c_B z^2/2}, \quad (3.19)$$

$$\sigma_3 \equiv \sigma_{y_1Y_2} = \frac{1}{2\pi\alpha'} \left(\frac{L^2 \mathfrak{b}_s(z)}{z^2} \right) \sqrt{\mathfrak{g}_2 \mathfrak{g}_3} = \frac{1}{2\pi\alpha'} \left(\frac{L^{2/\nu} \mathfrak{b}_s(z)}{z^{2/\nu}} \right) e^{c_B z^2/2}, \quad (3.20)$$

where $z = z_h$ or $z = z_{DW}$.

4 Numerical results

We study the position of the DW for effective potentials to investigate the spatial string tension and phase transition of string at different configurations. The effective potentials depend on the orientation. For particular orientations xY_1 , xY_2 and y_1Y_2 the effective potentials denoted by \mathcal{V}_1 , \mathcal{V}_2 and \mathcal{V}_3 are given by equations (3.18), (3.19) and (3.20), respectively. Although the effective potential depends on the parameters c , z_0 , z_h , and c_B , it does not depend on the chemical potential μ .

4.1 Spatial Wilson loop \mathcal{W}_{xY_1}

4.1.1 Zero-boundary condition

In this section the behavior of the effective potential \mathcal{V}_1 as a function of the holographic coordinate z corresponding to the first orientation of SWL, i.e. \mathcal{W}_{xY_1} , for different values of magnetic coefficients c_B is presented in Fig. 2 using the zero-boundary condition (2.10). Fig. 2 shows that \mathcal{V}_1 has local minimum, thus confirming $\mathcal{V}'(z) = 0$, i.e. the dynamical walls exist in the isotropic case $\nu = 1$ and in the anisotropic case $\nu = 4.5$ with different values of the magnetic coefficient c_B .

The locations of the dynamical walls for $\nu = 1$ and $\nu = 4.5$ with different values of c_B and are given in the Tables 1 and 2, respectively.

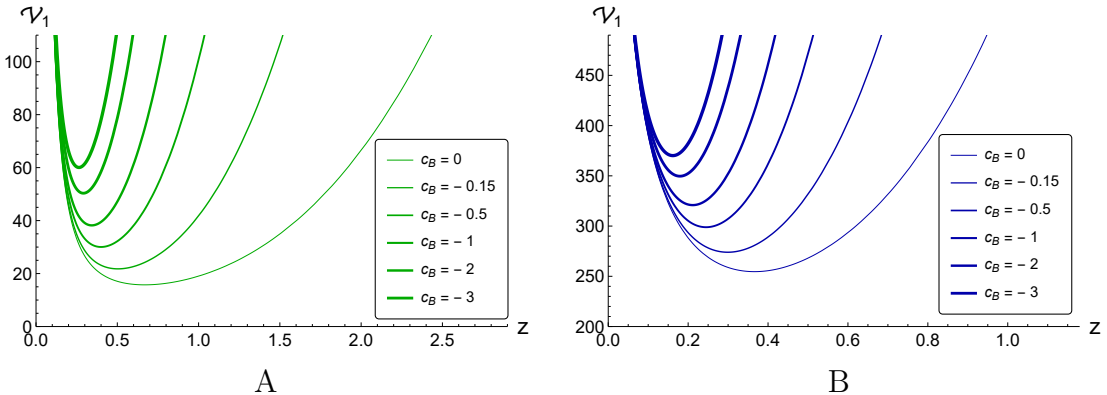


Figure 2. Effective potential $\mathcal{V}_1(z)$ in the first orientation \mathcal{W}_{xY_1} at (A) $\nu = 1$, and (B) $\nu = 4.5$ for different c_B considering zero-boundary condition (2.10); $[z]^{-1} = [c_B]^{1/2} = \text{GeV}$.

\mathcal{V}_1	$\nu = 1$					
$-c_B$	0	0.15	0.5	1	2	3
z_{DW}	0.665	0.500	0.400	0.341	0.285	0.261

Table 1. Locations of the dynamical walls z_{DW} for \mathcal{V}_1 in the first orientation \mathcal{W}_{xY_1} at $\nu = 1$, considering zero-boundary condition (2.10); $[z]^{-1} = [c_B]^{1/2} = \text{GeV}$.

\mathcal{V}_1	$\nu = 4.5$					
	$-c_B$	0	0.15	0.5	1	2
z_{DW}	0.366	0.300	0.245	0.212	0.180	0.162

Table 2. Locations of the dynamical walls z_{DW} for \mathcal{V}_1 in the first orientation \mathcal{W}_{xY_1} at $\nu = 4.5$, considering zero-boundary condition (2.10); $[z]^{-1} = [c_B]^{\frac{1}{2}} = \text{GeV}$.

The SWL string tension can be obtained by calculating the minimal value of the effective potential at the DW $z = z_{DW}$ or at the horizon $z = z_h$. Figs. 3 and 4 show the spatial string tension σ_1 as a function of temperature T for the first orientation of SWL, i.e. \mathcal{W}_{xY_1} , at $\mu = 0$, $\mu = 0.5 \text{ GeV}$ and $\mu = 1 \text{ GeV}$ for different c_B in the isotropic case $\nu = 1$ and the anisotropic case $\nu = 4.5$, respectively. Both figures were obtained considering the zero-boundary condition (2.10), and the cyan lines present the dependence of $\sigma(z_{DW})$ on temperature in the DW configuration, while the green and blue lines present the dependence of $\sigma(z_h)$ on temperature in the horizon configuration.

The phase transition occurs at critical temperature T_{cr} between two connected string configurations, i.e. DW and horizon configurations (see Fig. 25), with different values of spatial string tension: $\sigma(z_{DW})$ and $\sigma(z_h)$, respectively (see also Sect. 3.1). Note that this is a continuous phase transition. For this phase transition the string tension receives a large change in its value at the critical temperature T_{cr} . To put it in another way, the second derivative of the spatial string tension with respect to temperature $\partial^2\sigma/\partial T^2$ undergoes a jump. To compare this phase transition obtained from SWL with confinement/deconfinement and 1st order phase transitions, see Sect. 6 and Fig. 24.

Fig. 4 shows, that the spatial string tension σ value increases with the spatial anisotropy ν and the external magnetic field c_B . Here and below “larger magnetic field” means “larger absolute value of c_B ”. In addition, Figs. 3 and 4 show, that at lower temperature $T < T_{cr}$, i.e. in DW configuration, the spatial string tension does not depend on the temperature and gets a constant value such as $\sigma_1 = 60 \text{ GeV}^2$ for $\mu = 0$, $c_B = -3 \text{ GeV}^2$. Note also, that the DW coordinates are independent from the chemical potential. However, for $\mu = 0$, $c_B = 0$ Figs. 3A and 4A show, that for very low T the σ_1 does not exist due to lack of the DW coordinate.

Fig. 5 shows, that at fixed chemical potential the increasing magnetic coefficient c_B increases the transition temperature between the DW and the horizon configuration, thus confirming the magnetic catalysis phenomenon. Furthermore, inclusion of spatial anisotropy $\nu = 4.5$ decreases the critical transition temperature T_{cr} between the DW and the horizon configuration for all values of the magnetic field coefficient c_B in our model.

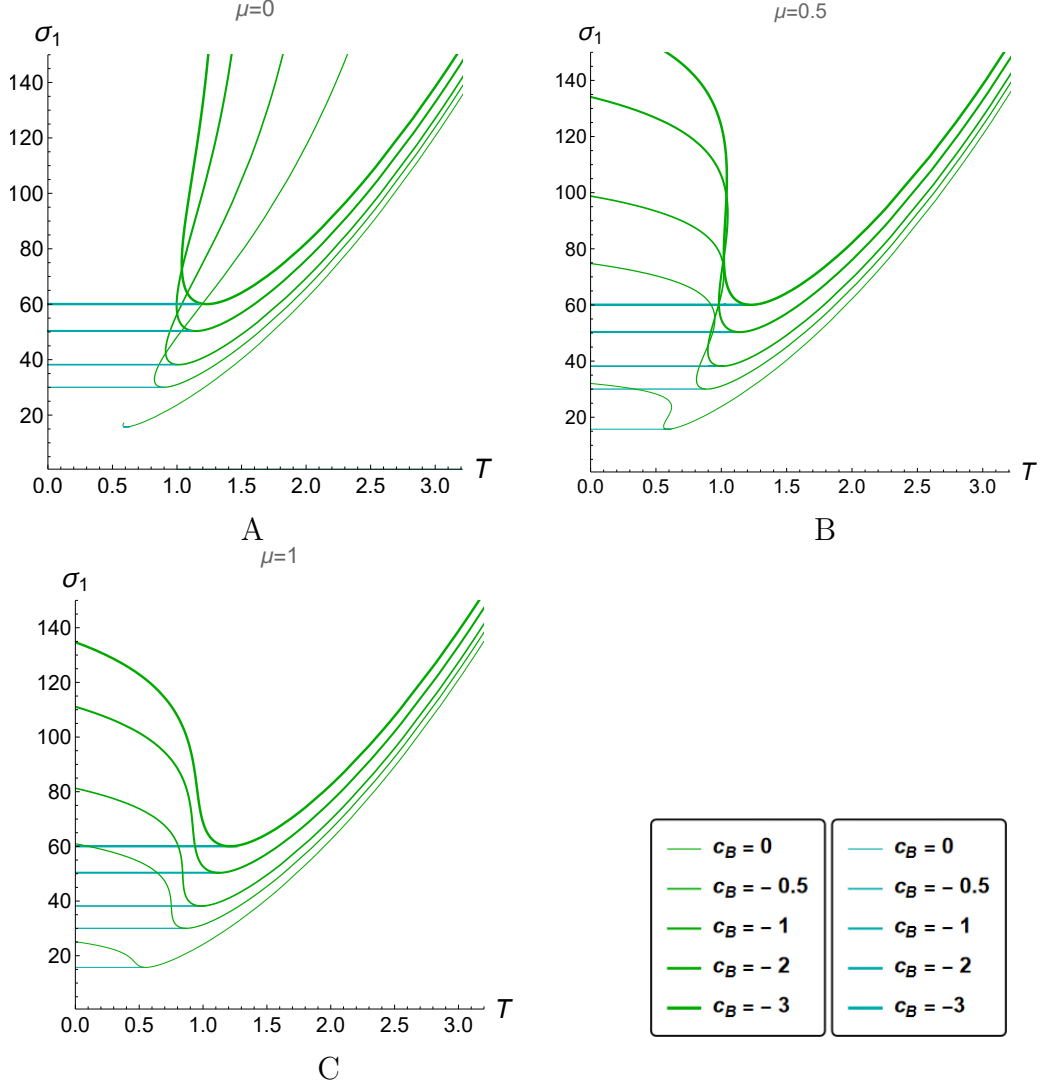


Figure 3. Spatial string tension σ_1 in the first orientation \mathcal{W}_{xY_1} as a function of temperature T for isotropic case $\nu = 1$ at (A) $\mu = 0$, (B) $\mu = 0.5$ GeV, and (C) $\mu = 1$ GeV with different c_B considering zero-boundary condition (2.10). The cyan line and green curve show DW and horizon configuration, respectively; $[\sigma]^{\frac{1}{2}} = [T] = [\mu] = [c_B]^{\frac{1}{2}} = \text{GeV}$.

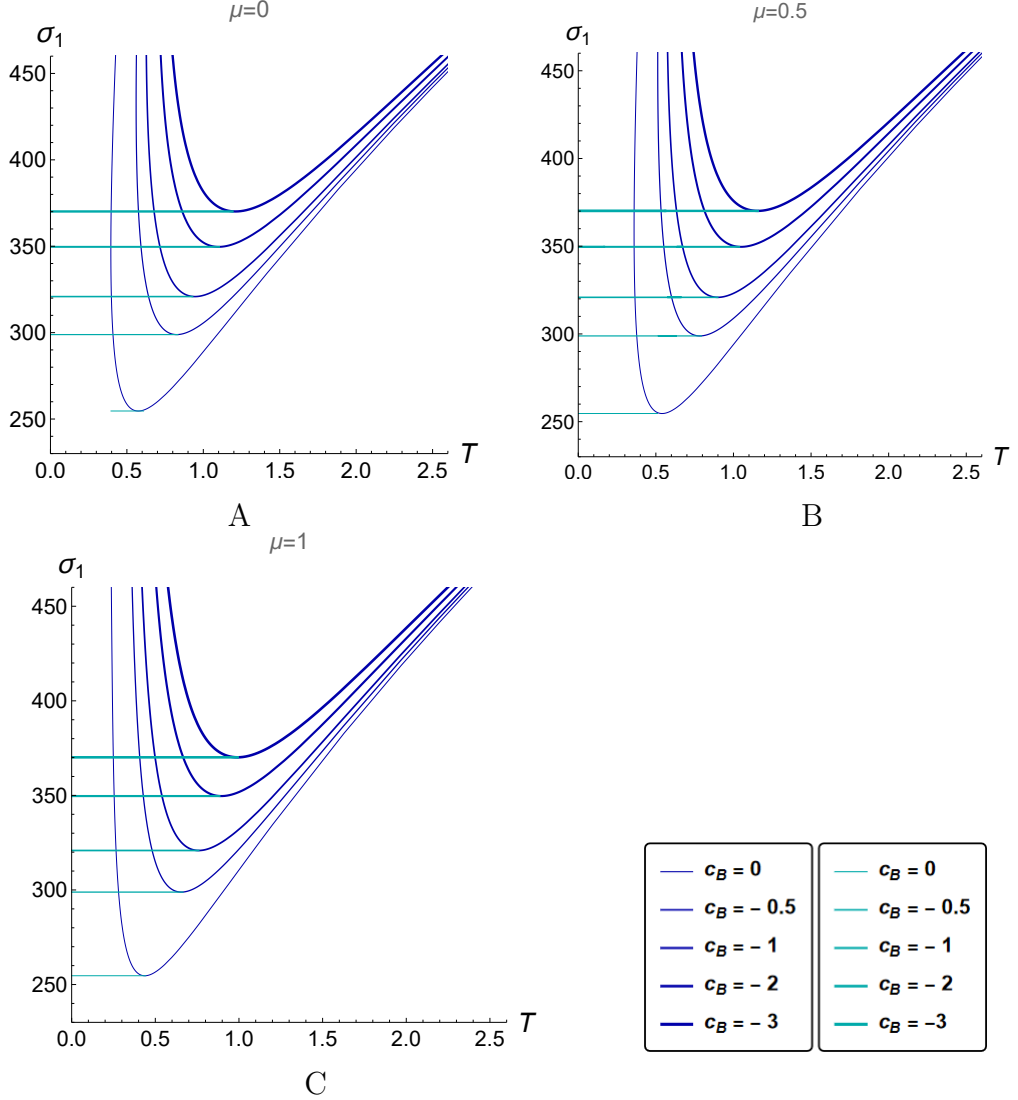


Figure 4. Spatial string tension σ_1 in the first orientation \mathcal{W}_{xY_1} as a function of temperature T for anisotropic case $\nu = 4.5$ at (A) $\mu = 0$, (B) $\mu = 0.5$ GeV, and (C) $\mu = 1$ GeV with different c_B considering zero-boundary condition (2.10). The cyan line and blue curve show DW and horizon configuration, respectively; $[\sigma]^{1/2} = [T] = [\mu] = [c_B]^{1/2} = \text{GeV}$.

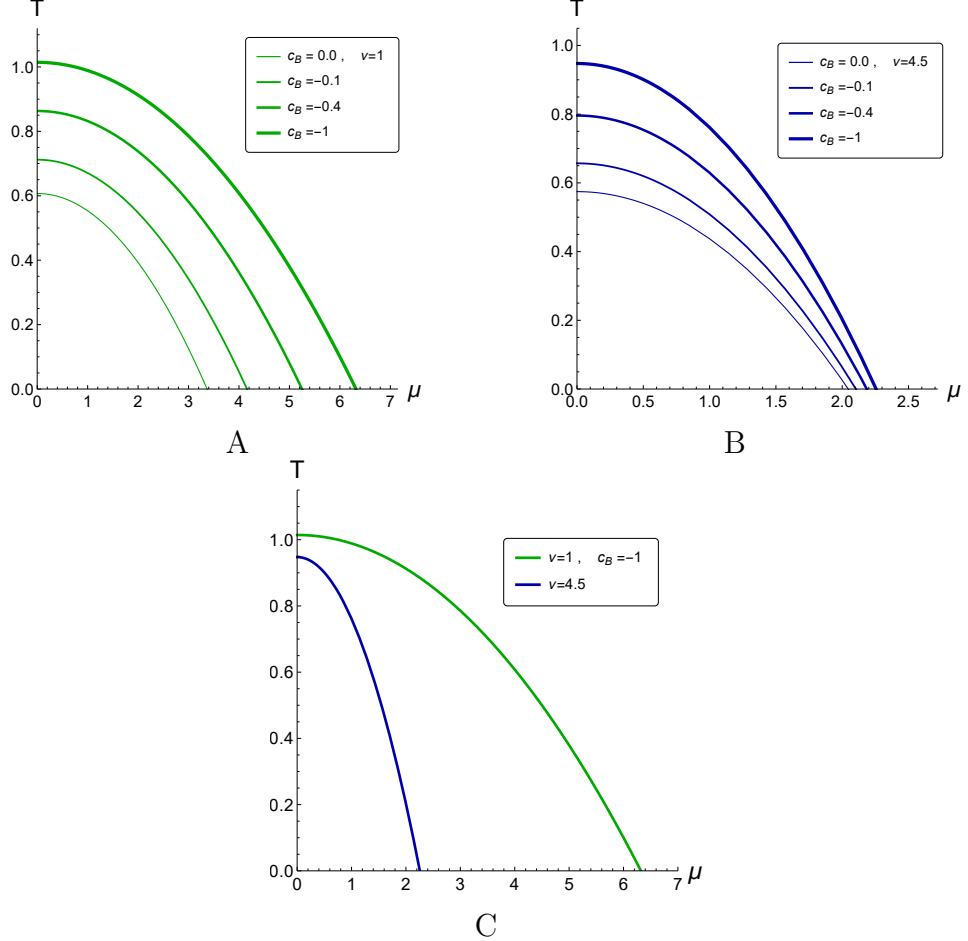


Figure 5. Phase transition diagrams in (μ, T) -plane in the first orientation \mathcal{W}_{xY_1} at (A) $\nu = 1$, (B) $\nu = 4.5$, and (C) comparison between $\nu = 1$ and $\nu = 4.5$ at fixed $c_B = -1$ GeV 2 corresponding to the transition from the DW configuration to the horizon configuration of σ_1 considering zero-boundary condition (2.10); $[T] = [\mu] = [c_B]^{\frac{1}{2}} = \text{GeV}$.

4.1.2 Physical-boundary condition

In this section we apply the physical-boundary condition (2.12) to the dilaton field to calculate the DW coordinate and the spatial string tension. We would like to compare the results of this subsection and those of subsection (4.1.1).

The behavior of the effective potential \mathcal{V}_1 as a function of holographic coordinate z for $\nu = 1$ and $\nu = 4.5$ corresponding to the first SWL orientation \mathcal{W}_{xY_1} for different values of the magnetic field coefficients c_B considering the physical-boundary condition (2.12) is presented in Fig. 6. This figure shows, that there is a minimum effective potential not only for the zero-boundary condition (2.10), but also for physical-boundary conditions (2.12).

The locations of the dynamical walls for different values of the magnetic co-

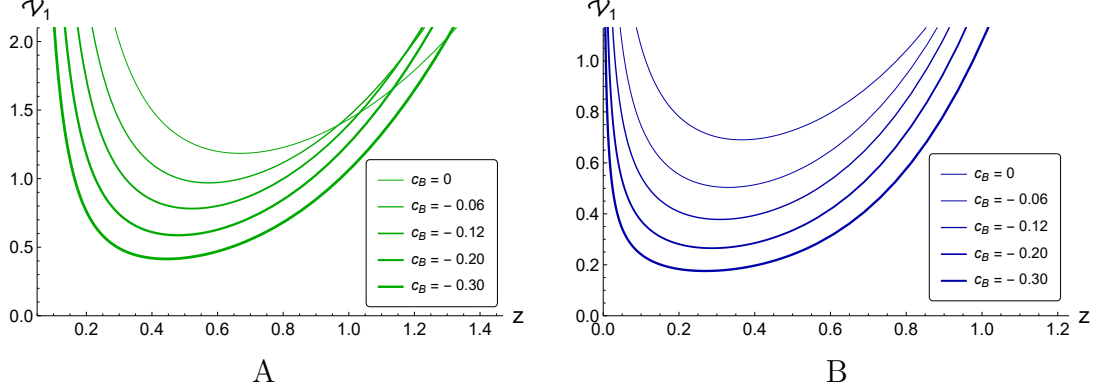


Figure 6. Effective potential $\mathcal{V}_1(z)$ in the first orientation \mathcal{W}_{xy1} at (A) $\nu = 1$, and (B) $\nu = 4.5$ for different c_B considering physical-boundary condition (2.12); $[z]^{-1} = [c_B]^{\frac{1}{2}} = \text{GeV}$.

efficient c_B in the isotropic case $\nu = 1$ and the anisotropic case $\nu = 4.5$ for the physical-boundary condition are given in the Tables 3 and 4, respectively.

Figs. 7 and 8 show spatial string tension σ_1 as a function of temperature T at $\mu = 0$, $\mu = 0.5$ GeV, and $\mu = 1$ GeV with different c_B for the isotropic case $\nu = 1$ and anisotropic case $\nu = 4.5$, respectively. In this case we considered the physical-boundary condition (2.10). The cyan line shows the dependence of σ in the DW configuration $\sigma(z_{DW})$ on temperature, and the green curve shows the dependence of $\sigma(z_h)$ in the horizon configuration on temperature.

In contradistinction to the zero-boundary condition (2.10), for physical-boundary condition Figs. 7 and 8 show, that inclusion of spatial anisotropy $\nu = 4.5$ and increasing the magnetic field c_B decreases the spatial string tension. However, for both zero- and physical-boundary conditions, the magnetic catalysis behavior was obtained. The DW coordinates are independent from the chemical potential. However, in the case of $\mu = 0$ for very low T in all values of c_B Figs. 7A and 8A show

\mathcal{V}_1	$\nu = 1$				
$-c_B$	0	0.06	0.12	0.2	0.3
z_{DW}	0.665	0.572	0.521	0.480	0.442

Table 3. Locations of dynamical walls z_{DW} , for \mathcal{V}_1 in the first orientation \mathcal{W}_{xy1} at $\nu = 1$ with different c_B for physical-boundary condition (2.12); $[z]^{-1} = [c_B]^{\frac{1}{2}} = \text{GeV}$.

\mathcal{V}_1	$\nu = 4.5$				
$-c_B$	0	0.06	0.12	0.2	0.3
z_{DW}	0.366	0.330	0.309	0.288	0.270

Table 4. Locations of dynamical walls z_{DW} , for \mathcal{V}_1 in the first orientation \mathcal{W}_{xy1} at $\nu = 4.5$ with different c_B for physical-boundary condition (2.12); $[z]^{-1} = [c_B]^{\frac{1}{2}} = \text{GeV}$.

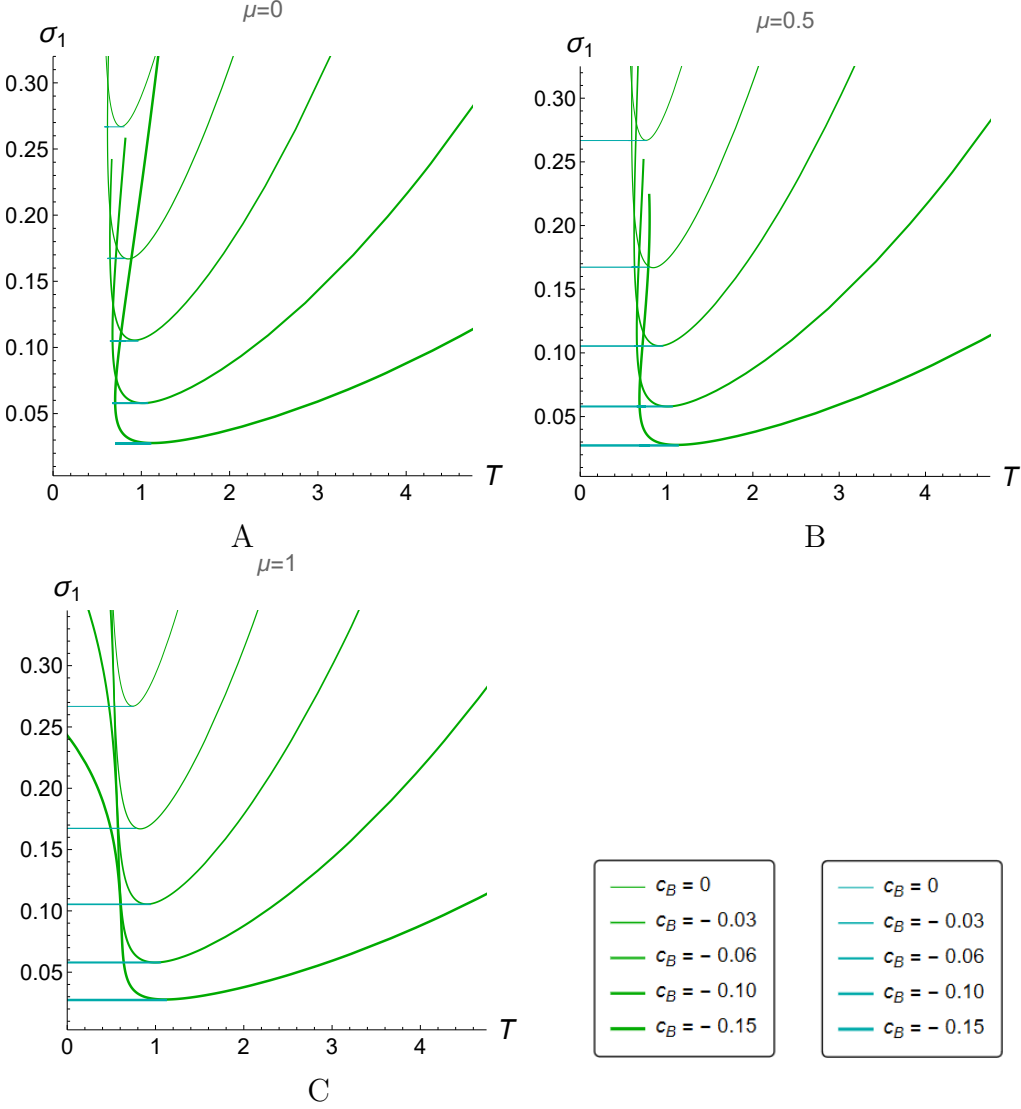


Figure 7. Spatial string tension σ_1 in the first orientation \mathcal{W}_{xY_1} as a function of temperature T for isotropic case $\nu = 1$ at (A) $\mu = 0$, (B) $\mu = 0.5$ GeV, and (C) $\mu = 1$ GeV with different c_B considering physical-boundary condition (2.10). The cyan line and green curve show DW and horizon configuration, respectively; $[\sigma]^{\frac{1}{2}} = [T] = [\mu] = [c_B]^{\frac{1}{2}} = \text{GeV}$.

that σ_1 does not exist due to lack of the DW coordinate. In the horizon configuration $T > T_{cr}$ for both the isotropic case $\nu = 1$ and the anisotropic case $\nu = 4.5$ the spatial string tension increases monotonically with temperature for zero- and physical-boundary conditions.

Comparison of Figs. 9 and 5 clearly shows, that the phase diagram does not depend on the boundary conditions. This result is confirmed by other models; see [77].

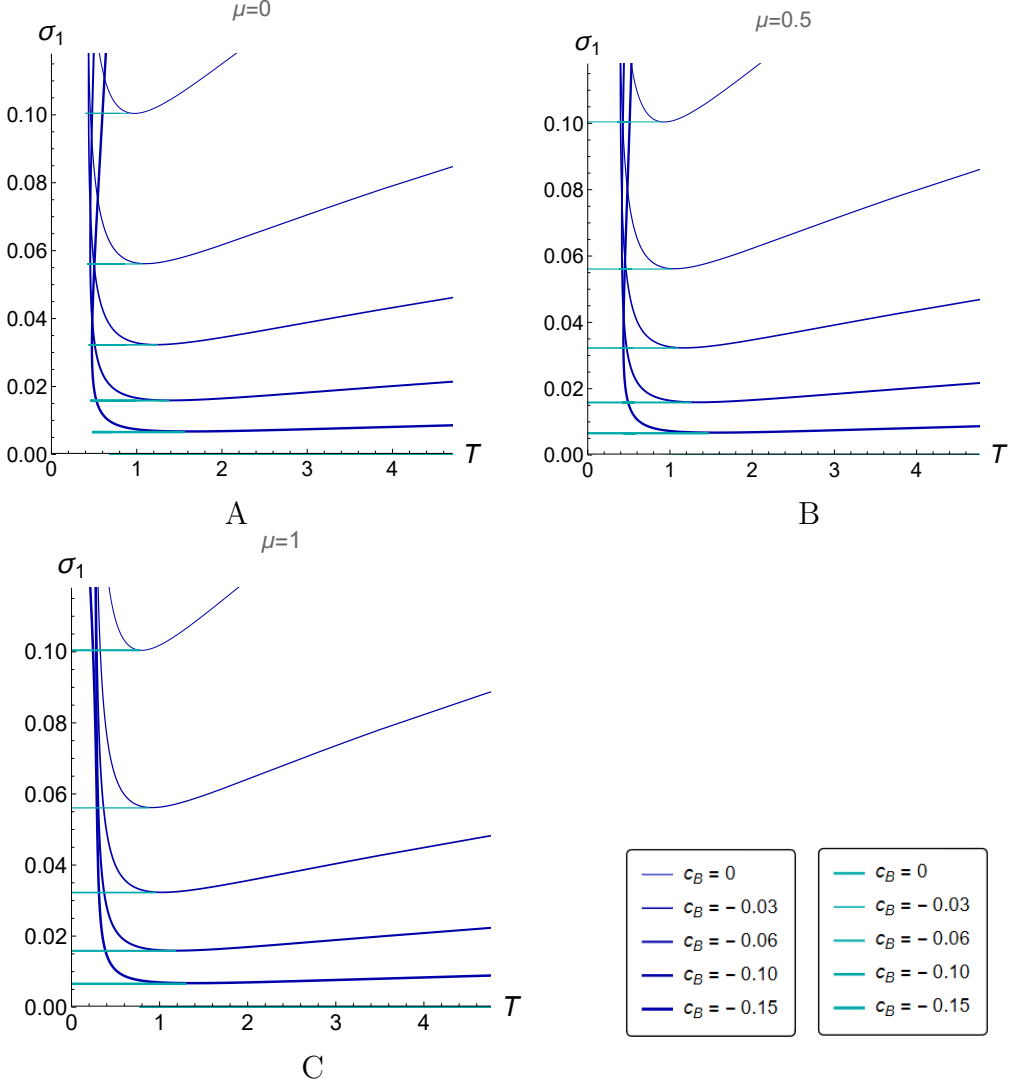


Figure 8. Spatial string tension σ_1 in the first orientation \mathcal{W}_{xY_1} as a function of temperature T for anisotropic case $\nu = 4.5$ at (A) $\mu = 0$, (B) $\mu = 0.5$ GeV, and (C) $\mu = 1$ GeV with different c_B considering physical-boundary condition (2.10). The cyan line and blue curve show DW and horizon configuration, respectively; $[\sigma]^{\frac{1}{2}} = [T] = [\mu] = [c_B]^{\frac{1}{2}} = \text{GeV}$.

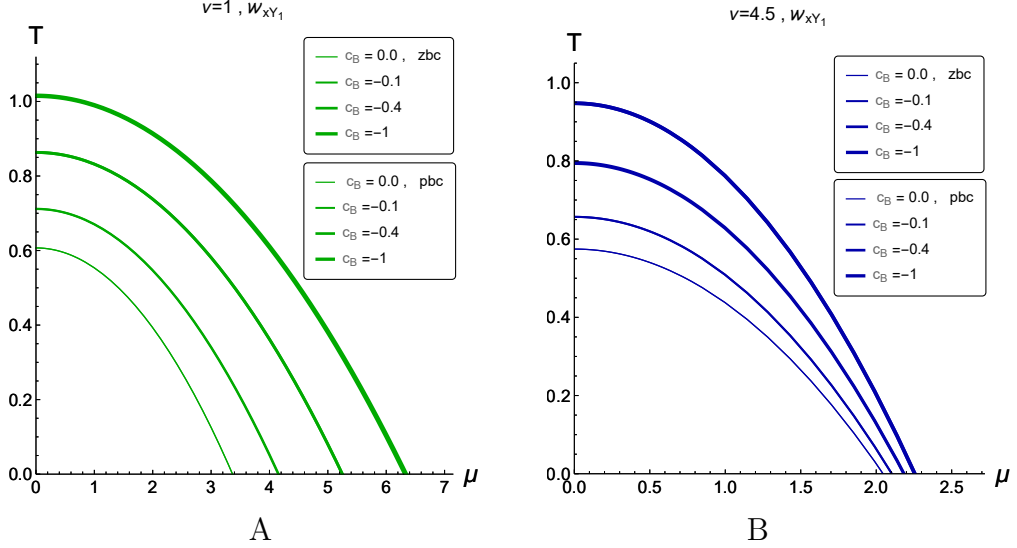


Figure 9. Phase transition diagrams in (μ, T) -plane in the first orientation \mathcal{W}_{xY_1} corresponding to the transition from the DW configuration to the horizon configuration of σ_1 at (A) $\nu = 1$, and (B) $\nu = 4.5$ with different c_B comparing the zero-boundary condition (zbc) (2.10) and physical-boundary condition (pbc) (2.12); $[T] = [\mu] = [c_B]^{\frac{1}{2}} = \text{GeV}$.

4.2 Spatial Wilson loop \mathcal{W}_{xY_2}

The behavior of the effective potential \mathcal{V}_2 as a function of the holographic coordinate z corresponding to the second orientation of the SWL, i.e. \mathcal{W}_{xY_2} for different values of magnetic coefficients c_B is presented in Fig. 10 using the zero-boundary condition (2.10). Fig. 10 shows, that \mathcal{V}_2 has local minimums thus confirming $\mathcal{V}'(z) = 0$, i.e. the dynamical walls exist at different values of the magnetic coefficient c_B for the isotropic and anisotropic cases $\nu = 1$ and $\nu = 4.5$, respectively.

Tables 5 and 6 show the DW locations at different values of the magnetic field c_B for $\nu = 1$ and $\nu = 4.5$, respectively.

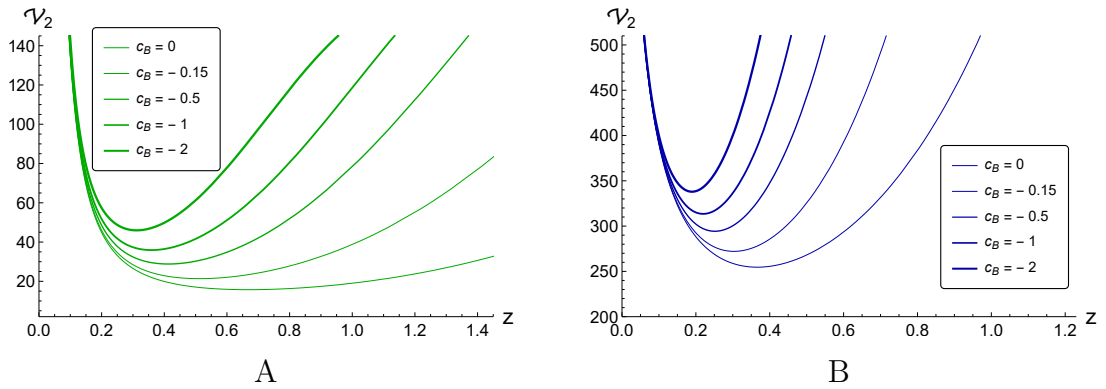


Figure 10. Effective potential $\mathcal{V}_2(z)$ in the second orientation \mathcal{W}_{xY_2} at (A) $\nu = 1$, and (B) $\nu = 4.5$ for different c_B considering zero-boundary condition (2.10); $[z]^{-1} = [c_B]^{\frac{1}{2}} = \text{GeV}$.

\mathcal{V}_2	$\nu = 1$				
$-c_B$	0	0.15	0.5	1	2
z_{DW}	0.665	0.515	0.415	0.360	0.315

Table 5. Locations of dynamical walls z_{DW} , for \mathcal{V}_2 in the second orientation \mathcal{W}_{xY_2} at $\nu = 1$ considering zero-boundary condition (2.10); $[z]^{-1} = [c_B]^{\frac{1}{2}} = \text{GeV}$.

\mathcal{V}_2	$\nu = 4.5$				
$-c_B$	0	0.15	0.5	1	2
z_{DW}	0.366	0.305	0.250	0.220	0.190

Table 6. Locations of dynamical walls z_{DW} , for \mathcal{V}_2 in the second orientation \mathcal{W}_{xY_2} at $\nu = 4.5$ considering zero-boundary condition (2.10); $[z]^{-1} = [c_B]^{\frac{1}{2}} = \text{GeV}$.

Figs. 11 and 12 depict the spatial string tension σ_2 as a function of temperature T in $\mu = 0$, $\mu = 0.5 \text{ GeV}$, and $\mu = 1 \text{ GeV}$ with different c_B for the isotropic case $\nu = 1$ and anisotropic case $\nu = 4.5$, respectively. The cyan lines present the dependence of $\sigma(z_{DW})$ on temperature in the DW configuration, while the green and blue lines present the dependence of $\sigma(z_h)$ on temperature in the horizon configuration.

Figs. 13A and 13B show the phase diagrams in the (μ, T) -plane for σ_2 in the second orientation \mathcal{W}_{xY_2} corresponding to the transition from the DW configuration to the horizon configuration at zero-boundary condition (2.10) for $\nu = 1$ and $\nu = 4.5$, respectively. Fig. 13C shows, that inclusion of spatial anisotropy decreases T_{cr} .

The results of the spatial string tension as a function of T in the second SWL orientation \mathcal{W}_{xY_2} shown in Figs. 11 and 12 are the following.

- Exhibits the magnetic catalysis behavior, which T_{cr} increases by enhancing the magnetic field c_B .
- The spatial string tension σ increases as the spatial anisotropy ν , and the external magnetic field c_B increases.
- At lower temperature $T < T_{cr}$ is in the DW configuration, the string tension does not depend on the temperature and gets a constant value such as $\sigma_2 = 46 \text{ GeV}^2$ at $\mu = 0$ and $c_B = -2 \text{ GeV}^2$.
- At higher temperature $T > T_{cr}$ in the horizon configuration, the string tension increases monotonically.
- The DW coordinates are independent of the chemical potential.

Note that comparing the phase diagrams between the first SWL orientation \mathcal{W}_{xY_1} and the second orientation \mathcal{W}_{xY_2} is investigated in Sect. 4.4.

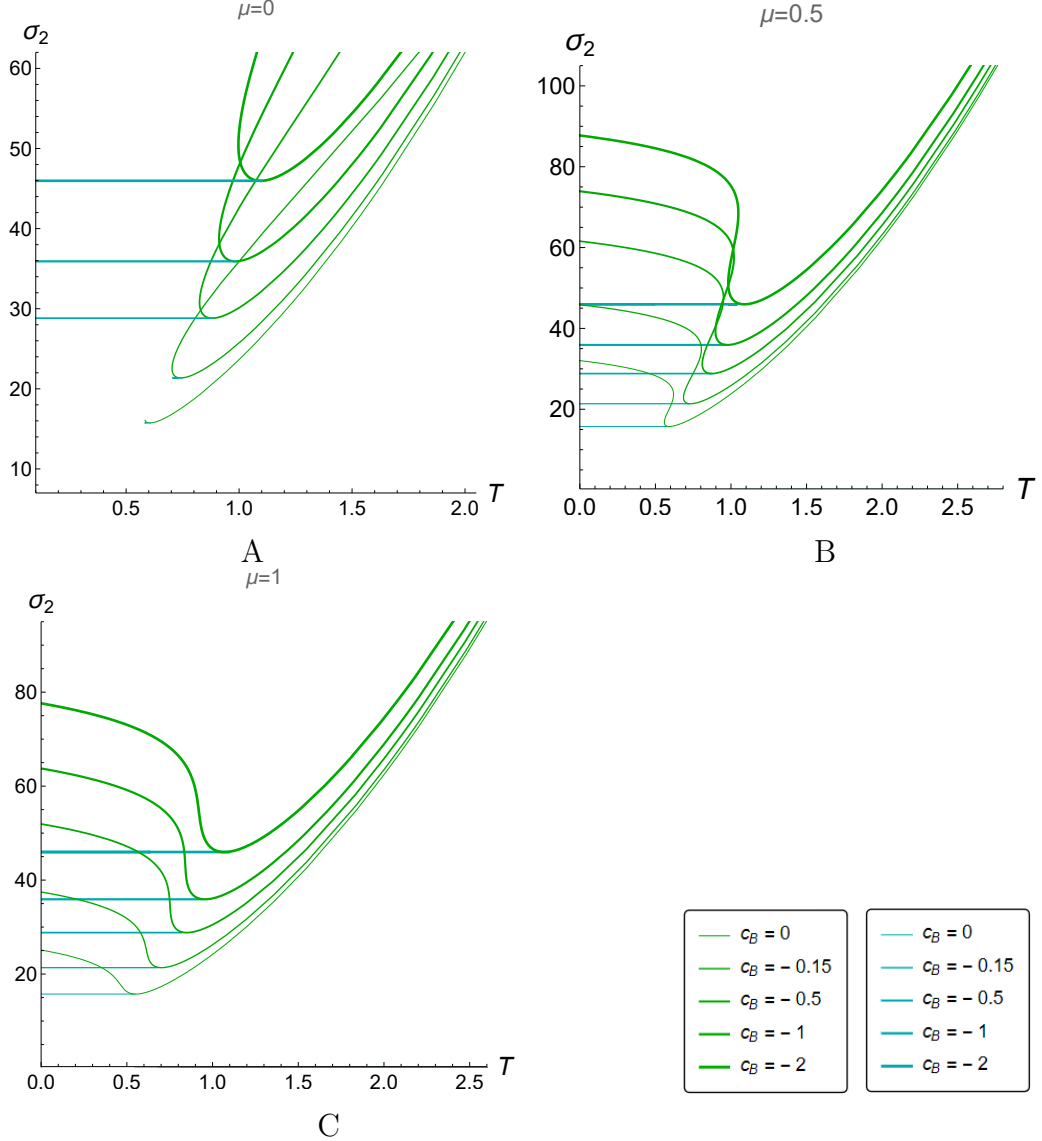


Figure 11. Spatial string tension σ_2 in the second orientation \mathcal{W}_{xY_2} as a function of temperature T for isotropic case $\nu = 1$ at (A) $\mu = 0$, (B) $\mu = 0.5$ GeV, and (C) $\mu = 1$ GeV with different c_B considering zero-boundary condition (2.10). The cyan line and green curve show DW and horizon configuration, respectively; $[\sigma]^{1/2} = [T] = [\mu] = [c_B]^{1/2} = \text{GeV}$.

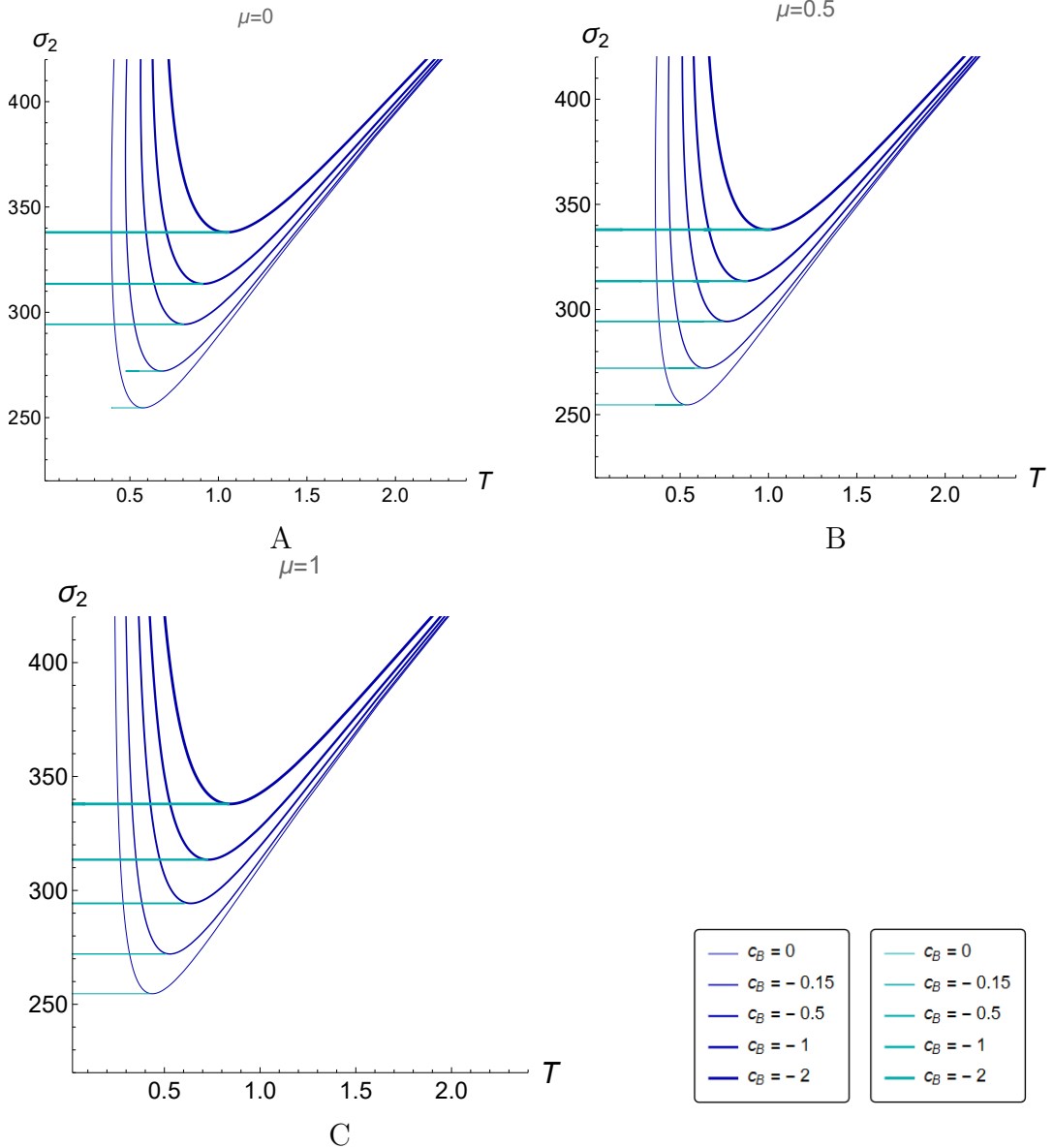


Figure 12. Spatial string tension σ_2 in the second orientation \mathcal{W}_{xY_2} as a function of temperature T for anisotropic case $\nu = 4.5$ at (A) $\mu = 0$, (B) $\mu = 0.5$ GeV, and (C) $\mu = 1$ GeV with different c_B considering zero-boundary condition (2.10). The cyan line and blue curve show DW and horizon configuration, respectively; $[\sigma]^{1/2} = [T] = [\mu] = [c_B]^{1/2} = \text{GeV}$.

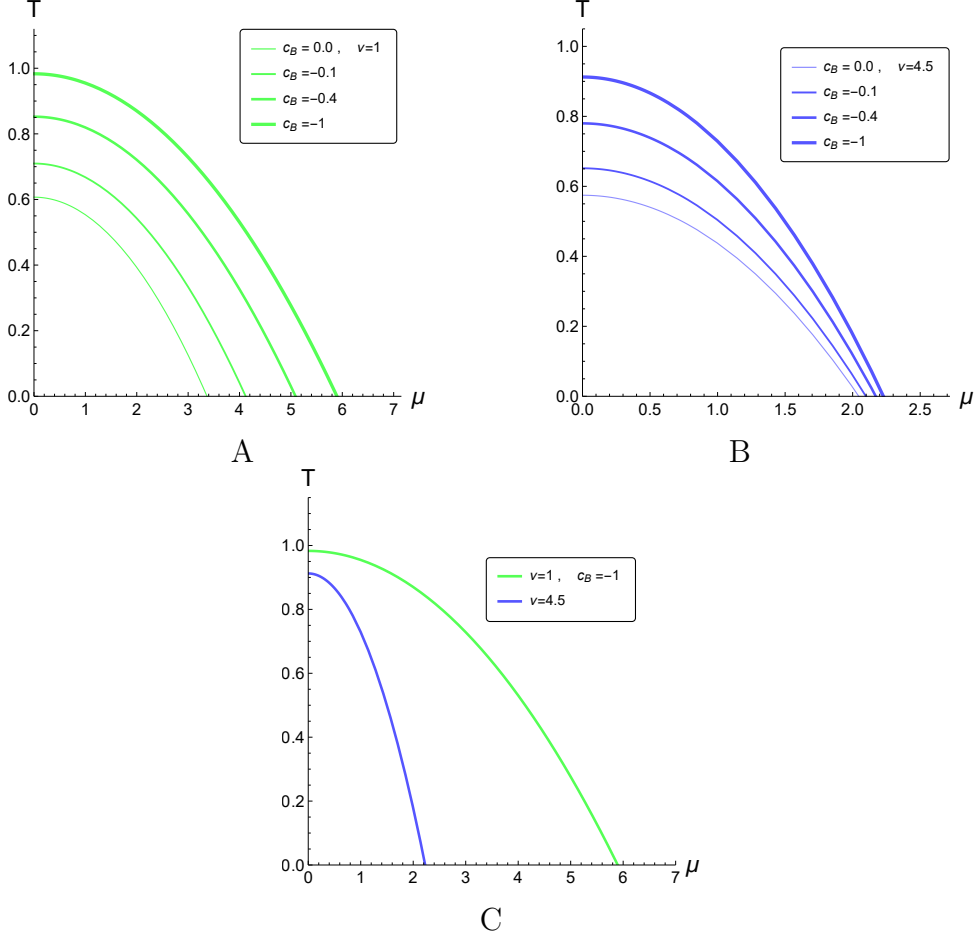


Figure 13. Phase diagrams in (μ, T) -plane at (A) $\nu = 1$, (B) $\nu = 4.5$, and (C) comparison between $\nu = 1$ and $\nu = 4.5$ at fixed $c_B = -1$ GeV 2 in the second orientation $\mathcal{W}_{y_1 Y_2}$, corresponding to the transition from the DW configuration to the horizon configuration of σ_2 considering zero-boundary condition (2.10); $[T] = [\mu] = [c_B]^{\frac{1}{2}} = \text{GeV}$.

4.3 Spatial Wilson loop $\mathcal{W}_{y_1 Y_2}$

The third SWL orientation, i.e. $\mathcal{W}_{y_1 Y_2}$, has very peculiar characteristics compared to the first orientation $\mathcal{W}_{x Y_1}$ and the second orientation $\mathcal{W}_{x Y_2}$.

The effective potential $\mathcal{V}_3(z)$ in the third orientation $\mathcal{W}_{y_1 Y_2}$ for $\nu = 1$ and $\nu = 4.5$ in different c_B considering the zero-boundary condition (2.10) is shown in Fig. 14. In $\nu = 1$, Fig. 14A, the effective potential curves and the DW coordinates are exactly the same as the results of the second SWL orientation $\mathcal{W}_{x Y_2}$, that is clear from equations (3.19) and (3.20). However, for $\nu = 1$ there are DW coordinates, but for $\nu = 4.5$, Fig. 14B, the curves of the effective potential have no minimum and therefore no DW coordinates.

It is important to note that the third SWL orientation $\mathcal{W}_{y_1 Y_2}$ in the anisotropic

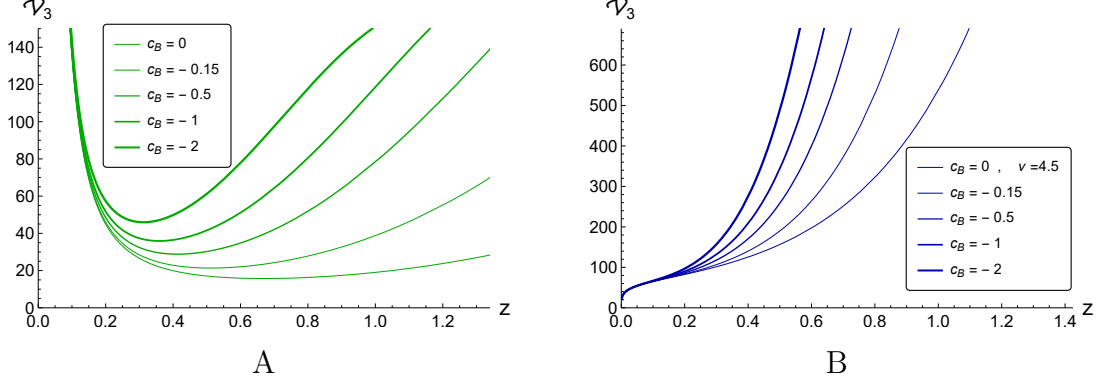


Figure 14. Effective potential $\mathcal{V}_3(z)$ in the third orientation $\mathcal{W}_{y_1Y_2}$ for different anisotropies (A) $\nu = 1$, and (B) $\nu = 4.5$ at different c_B considering zero-boundary condition (2.10); $[z]^{-1} = [c_B]^{\frac{1}{2}} = \text{GeV}$.

system has a different characteristic compared to other orientations. We found that there is a critical value of anisotropy $\nu_{cr} = 2.5$, where the DW coordinates disappear. To see this feature, in Fig. 15A the effective potential $\mathcal{V}_3(z)$ in the third orientation $\mathcal{W}_{y_1Y_2}$ for fixed value of the magnetic field $c_B = -1 \text{ GeV}^2$ and different ν considering the zero-boundary condition (2.10) is shown. In Fig. 15B, the critical value of anisotropy $\nu_{cr} = 2.5$ is depicted in zoomed mode. For $\nu \geq 2.5$ there are no DW coordinates in the system and therefore no spatial string tension.

Due to the existence of ν_{cr} in the third SWL orientation $\mathcal{W}_{y_1Y_2}$ we should consider anisotropy $\nu < 2.5$ to investigate the DW coordinate and spatial string tension. We choose $\nu = 2$ and depict the potential $\mathcal{V}_3(z)$ at different values of magnetic field c_B considering the zero-boundary condition (2.10) in Fig. 16. The minimum of the curves in Fig. 16 determines the DW coordinates presented in Table 7 for $\nu = 2$.

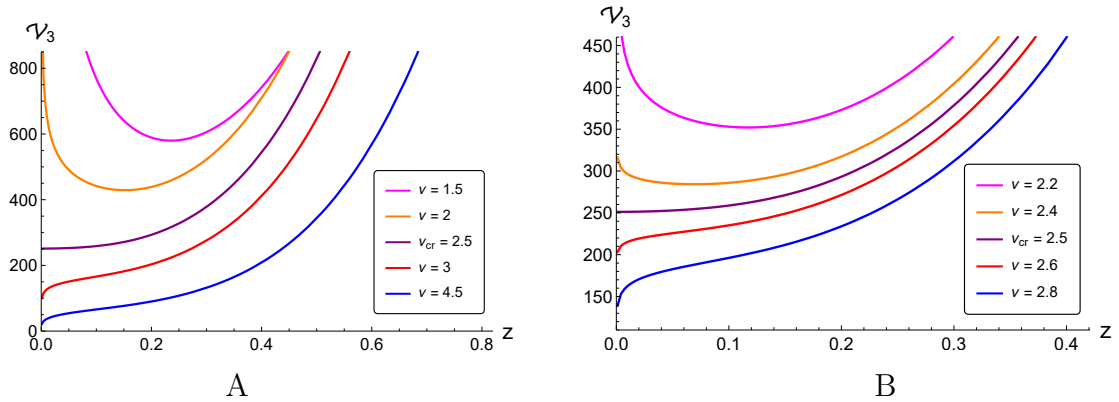


Figure 15. Effective potential $\mathcal{V}_3(z)$ in the third orientation $\mathcal{W}_{y_1Y_2}$ at fixed value of magnetic field $c_B = -1$ for (A) different anisotropies ν , and (B) zoom of panel (A) around the critical value of spatial anisotropy $\nu_{cr} = 2.5$ considering zero-boundary condition (2.10); $[z]^{-1} = [c_B]^{\frac{1}{2}} = \text{GeV}$.

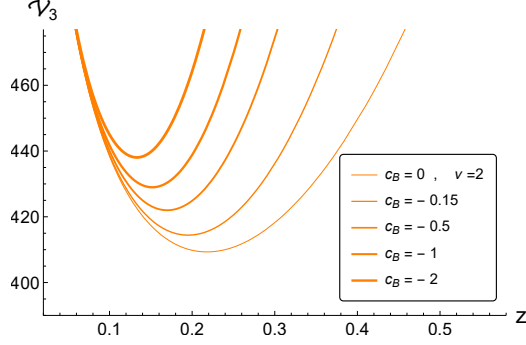


Figure 16. Effective potential $\mathcal{V}_3(z)$ in the third orientation $\mathcal{W}_{y_1Y_2}$ for $\nu = 2$ at different values of magnetic field c_B considering zero-boundary condition (2.10); $[z]^{-1} = [c_B]^{\frac{1}{2}} = \text{GeV}$.

\mathcal{V}_3	$\nu = 2$					
	$-c_B$	0	0.15	0.5	1	2
z_{DW}	0.218	0.195	0.170	0.152	0.133	

Table 7. Locations of dynamical walls z_{DW} , for \mathcal{V}_3 in the third orientation $\mathcal{W}_{y_1Y_2}$ at $\nu = 2$ considering zero-boundary condition (2.10); $[z]^{-1} = [c_B]^{\frac{1}{2}} = \text{GeV}$.

Fig. 17 shows the spatial string tension σ_3 as a function of temperature T for the anisotropic case $\nu = 2$ in the third SWL orientation $\mathcal{W}_{y_1Y_2}$ at $\mu = 0, \mu = 0.5 \text{ GeV}$ and $\mu = 1 \text{ GeV}$ and different magnetic fields c_B considering the zero-boundary condition (2.10). The cyan lines present the dependence of $\sigma(z_{DW})$ on temperature in the DW configuration, while the orange lines present the dependence of $\sigma(z_h)$ on temperature in the horizon configuration. The spatial string tension exhibits a constant value in the DW configuration at $T < T_{cr}$ such as $\sigma_3 = 438 \text{ GeV}^2$ at $\mu = 0$ and $c_B = -2 \text{ GeV}^2$. However, in the horizon configuration at $T > T_{cr}$ it increases monotonically.

Fig. 18A shows the phase diagrams in the (μ, T) -plane at $\nu = 2$, and Fig. 18B presents the comparison between $\nu = 1$ and $\nu = 2$ with fixed magnetic field $c_B = -1 \text{ GeV}^2$ in the third SWL orientation $\mathcal{W}_{y_1Y_2}$, corresponding to the transition from the DW configuration to the horizon configuration of σ_3 , considering the zero-boundary condition (2.10). Fig. 18A confirms the magnetic catalysis behavior at $\nu = 2$, and Fig. 18B shows that inclusion of anisotropy increases or decreases the transition temperature depending on μ in this case.

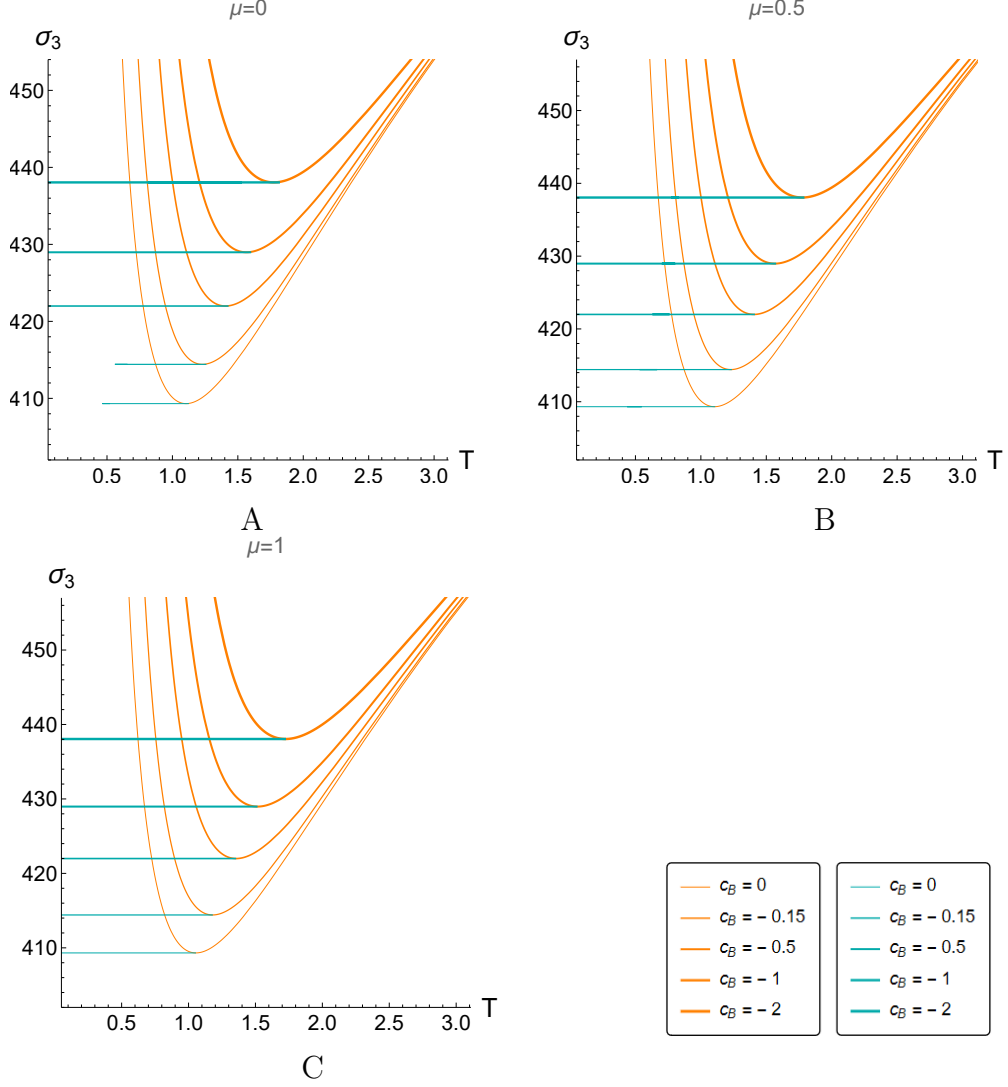


Figure 17. Spatial string tension σ_3 in the third orientation $\mathcal{W}_{y_1 Y_2}$ as a function of temperature T for isotropic case $\nu = 2$ at (A) $\mu = 0$, (B) $\mu = 0.5$ GeV, and (C) $\mu = 1$ GeV with different c_B considering zero-boundary condition (2.10). The cyan line and orange curve show DW and horizon configuration, respectively; $[\sigma]^{1/2} = [T] = [\mu] = [c_B]^{1/2} = \text{GeV}$.

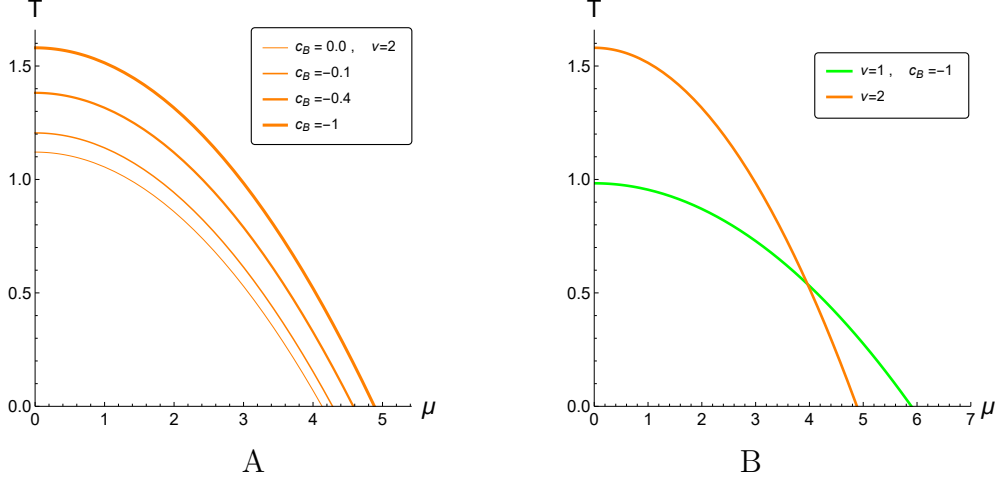


Figure 18. Phase diagrams in (μ, T) -plane at (A) $\nu = 2$, and (B) comparison between $\nu = 1$ and $\nu = 2$ at fixed $c_B = -1$ GeV 2 in the third orientation $\mathcal{W}_{y_1 Y_2}$, corresponding to the transition of σ_3 from the DW configuration to the horizon configuration, considering zero-boundary condition (2.10); $[T] = [\mu] = [c_B]^{\frac{1}{2}} = \text{GeV}$.

4.4 Phase diagrams in particular SWL orientations

Different orientations of SWL mean different embeddings of the string in the bulk. In addition, different embeddings lead to different physics [1], that is presented in Fig. 19.

To compare the phase diagrams in the (μ, T) -plane in the first $\mathcal{W}_{x Y_1}$ and second orientation $\mathcal{W}_{x Y_2}$ at $\nu = 1$, and (B) $\nu = 4.5$ Figs. 19A and 19B are presented, respectively. The transition temperature characterizes the phase transition between the DW configuration and the horizon configuration of σ_3 considering the zero-boundary condition (2.10). Our results reveal, that for the isotropic $\nu = 1$ and anisotropic $\nu = 4.5$ cases the transition temperature has lower values for the second SWL orientation $\mathcal{W}_{x Y_2}$ compared to the first orientation. Note that for $c_B = 0$ the phase transition curves coincide exactly as the values of σ for both orientations are the same, see (3.18) and (3.19).

In Fig. 20 the comparison of phase transition diagrams in the (μ, T) -plane at $\nu = 2$ among all three orientations, i.e. the first $\mathcal{W}_{x Y_1}$, the second $\mathcal{W}_{x Y_2}$ and the third orientation $\mathcal{W}_{y_1 Y_2}$, corresponding to the transition of σ_3 from the DW configuration to the horizon configuration at the zero-boundary condition (2.10) is shown. The result of Fig. 19 is confirmed for the first $\mathcal{W}_{x Y_1}$ and the second $\mathcal{W}_{x Y_2}$ orientations. In addition, Fig. 20 shows that the transition temperature has higher values for the third SWL orientation $\mathcal{W}_{y_1 Y_2}$ in comparison to the first and second ones for all values of the magnetic field c_B .

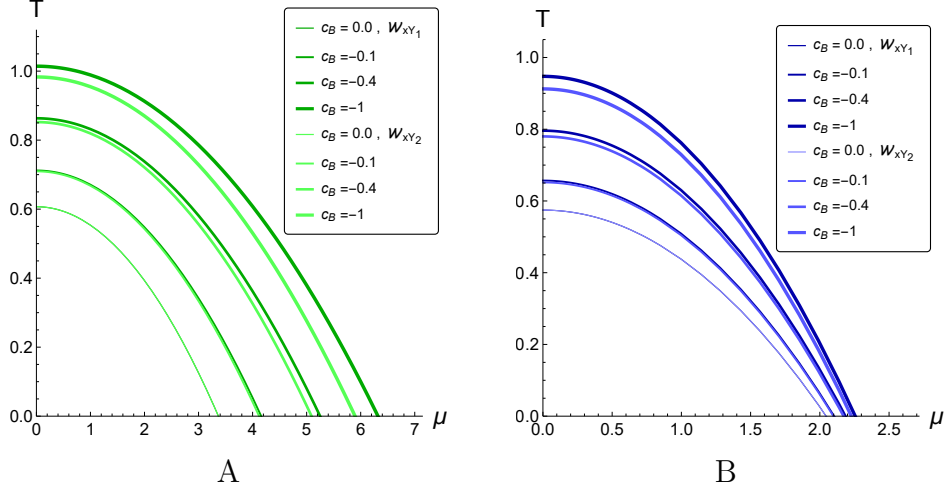


Figure 19. Phase diagrams in (μ, T) -plane at (A) $\nu = 1$, and (B) $\nu = 4.5$ in the first orientation \mathcal{W}_{xY_1} and the second orientation \mathcal{W}_{xY_2} , corresponding to the transition of σ_3 from the DW configuration to the horizon configuration considering zero-boundary condition (2.10); $[T] = [\mu] = [c_B]^{\frac{1}{2}} = \text{GeV}$.

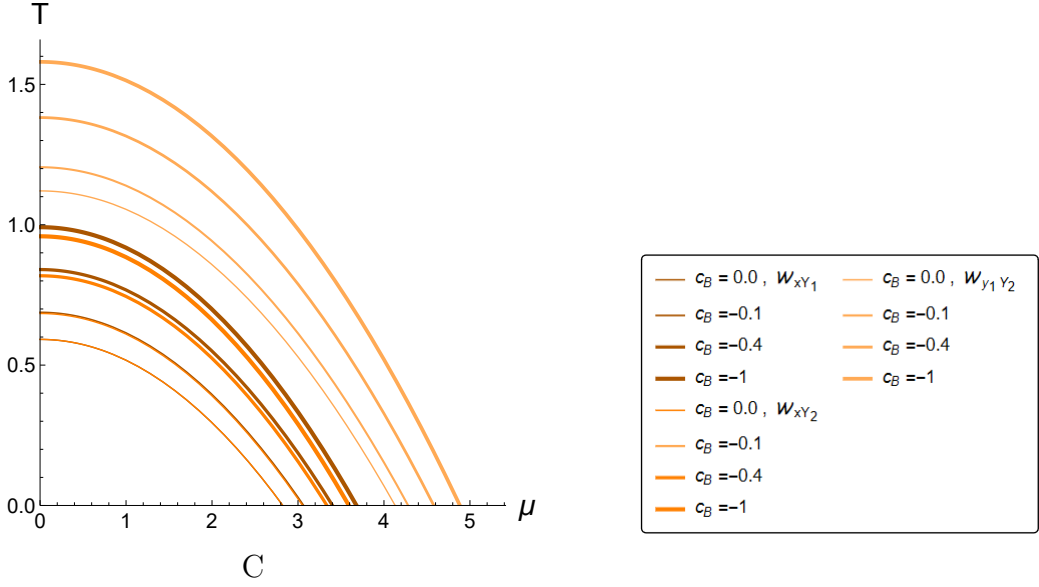


Figure 20. Phase transition diagrams in (μ, T) -plane at $\nu = 2$ for the first \mathcal{W}_{xY_1} , and the second \mathcal{W}_{xY_2} with the third orientation $\mathcal{W}_{y_1Y_2}$, corresponding to the transition of σ_3 from the DW configuration to the horizon configuration at zero-boundary condition (2.10); $[T] = [\mu] = [c_B]^{\frac{1}{2}} = \text{GeV}$.

5 Comparing the spatial string tension with lattice calculations

The connection between spatial string tensions and drag forces is remarkable. The drag force specifies the resistance that the heavy quark undergoes while moving through the hot and dense QGP. The drag force on the stretched string can describe the energy loss of the heavy quark [66, 67]. It was shown that in the strong coupling regime the drag force is proportional to the spatial string tension $\sigma \propto T^2$, where T denotes temperature [69, 70]. In addition, the temperature dependence of the spatial string tension is studied in more detail in [85].

Note that for the general metric (3.5) considering $\mathfrak{g}_1 = 1$ the drag forces on the heavy quarks in the x , y_1 , and y_2 directions have already been calculated in the anisotropic model [6] as

$$p_x = v_x \frac{\mathfrak{b}_s(z_h)}{z_h^2}, \quad (5.1)$$

$$p_{y_1} = v_{y_1} \frac{\mathfrak{b}_s(z_h)}{z_h^2} \mathfrak{g}_2(z_h), \quad (5.2)$$

$$p_{y_2} = v_{y_2} \frac{\mathfrak{b}_s(z_h)}{z_h^2} \mathfrak{g}_3(z_h). \quad (5.3)$$

If we take into account $L^2/\alpha' = \sqrt{\lambda}$ and identify

$$v_x = v \sqrt{\mathfrak{g}_2}, \quad (5.4)$$

$$v_{y_1} = v \frac{\sqrt{\mathfrak{g}_3}}{\mathfrak{g}_2}, \quad (5.5)$$

$$v_{y_2} = v \frac{\sqrt{\mathfrak{g}_2}}{\sqrt{\mathfrak{g}_3}}, \quad (5.6)$$

the drag forces (5.1)–(5.3) can reproduce spatial string tensions (3.18), (3.19), and (3.20) at $z = z_h$:

$$\sigma_{xY_1} \Big|_{z=z_h} = \frac{\sqrt{\lambda}}{2\pi} \left(\frac{\mathfrak{b}_s(z_h)}{z_h^2} \right) \sqrt{\mathfrak{g}_1 \mathfrak{g}_2}, \quad (5.7)$$

$$\sigma_{xY_2} \Big|_{z=z_h} = \frac{\sqrt{\lambda}}{2\pi} \left(\frac{\mathfrak{b}_s(z_h)}{z_h^2} \right) \sqrt{\mathfrak{g}_1 \mathfrak{g}_3}, \quad (5.8)$$

$$\sigma_{y_1 Y_2} \Big|_{z=z_h} = \frac{\sqrt{\lambda}}{2\pi} \left(\frac{\mathfrak{b}_s(z_h)}{z_h^2} \right) \sqrt{\mathfrak{g}_2 \mathfrak{g}_3} \quad (5.9)$$

for some constant v and $\mathfrak{g}_1 = 1$. Therefore, the spatial string tension is proportional to the drag force in the anisotropic medium.

It is interesting to investigate the temperature dependence of the spatial string tension. Taking $\mathfrak{g}_1 = 1$, $\mathfrak{g}_2(z_h) = (z_h/L)^{2-2/\nu}$, and $\mathfrak{g}_3(z_h) = (z_h/L)^{2-2/\nu}e^{c_B z_h^2}$, we have

$$\sigma_1 \equiv \sigma_{xY_1} \Big|_{z=z_h} = \frac{1}{2\pi\alpha'} \left(\frac{L^{1+1/\nu} \mathfrak{b}_s(z_h)}{z_h^{1+1/\nu}} \right), \quad (5.10)$$

$$\sigma_2 \equiv \sigma_{xY_2} \Big|_{z=z_h} = \frac{1}{2\pi\alpha'} \left(\frac{L^{1+1/\nu} \mathfrak{b}_s(z_h)}{z_h^{1+1/\nu}} \right) e^{c_B z_h^2/2}, \quad (5.11)$$

$$\sigma_3 \equiv \sigma_{y_1 Y_2} \Big|_{z=z_h} = \frac{1}{2\pi\alpha'} \left(\frac{L^{2/\nu} \mathfrak{b}_s(z_h)}{z_h^{2/\nu}} \right) e^{c_B z_h^2/2}. \quad (5.12)$$

Fig. 21A presents the string tension σ_1 in the first orientation \mathcal{W}_{xY_1} as a function of the temperature T at $\mu = 0$ for the isotropic case $\nu = 1$. The fitted solid red curve is $11.2 + 12.4 T^2$, and the fitted dashed red curve is $33.1 + 10.9 T^2$. Fig. 21B depicts the anisotropic case $\nu = 4.5$ at $\mu = 0$. The fitted solid red curve is $226.1 + 91.3 T^2 - 31.9 T^3 + 3.7 T^4$, and the fitted dashed red curve is $288.2 + 31.9 T^2 + 0.8 T^3 - 1.4 T^4$. Our result shows, that for the fully isotropic case $\nu = 1$ and $c_B = 0$ we have $\sigma_1 \propto T^2$ which is compatible with the result reported in [67, 69, 85] and also is qualitatively consistent with the lattice results [86, 87]. Inclusion of spatial anisotropy $\nu = 4.5$ clearly shows that the behavior of $\sigma(T)$ deviates from the quadratic term and requires higher terms.

Fig. 22A shows the temperature dependence of the string tension σ_2 in the second orientation \mathcal{W}_{xY_2} at $\mu = 0$ for the isotropic case $\nu = 1$. Fig. 22B presents the fitted solid red curve is $18.9 + 11.7 T^2$ and the fitted dashed red curve is $30.2 + 11.1 T^2$ for the anisotropic case $\nu = 4.5$ at $\mu = 0$, the fitted solid red curve is $258.3 + 58.1 T^2 - 13.6 T^3 + 0.9 T^4$ and the fitted dashed red curve is $303.6 + 26.7 T^2 + 1.3 T^3 - 1.1 T^4$. In the isotropic case $\nu = 1$ at different values of the magnetic field c_B we get $\sigma_2 \propto T^2$. Note that our results for non-zero magnetic field $c_B \neq 0$ are our prediction and can probably be checked with lattice calculations. For the anisotropic case $\nu = 4.5$ $\sigma(T)$ is proportional to the higher terms of T .

Applying equations (5.10)-(5.12) to the third orientation $\mathcal{W}_{y_1 Y_2}$ shows, that in the isotropic case $\nu = 1$ with different c_B the results for $\sigma(T)$ are the same as in the second orientation. Therefore, in Fig. 23 the temperature dependence of σ_3 is investigated only for the anisotropic case $\nu = 2$ at $\mu = 0$ and different c_B . The solid gray curve is $409.6 + 4.5 T^2 + 0.9 T^3 - 0.3 T^4$, and the dashed gray curve is $433.8 - 4.3 T^2 + 3.9 T^3 - 0.6 T^4$. Therefore, in this case $\sigma(T)$ deviates from the quadratic behavior in the presence of spatial anisotropy.

It is important to note that for all orientations inclusion of the external magnetic field and the spatial anisotropy enhances the string tension in the horizon configura-

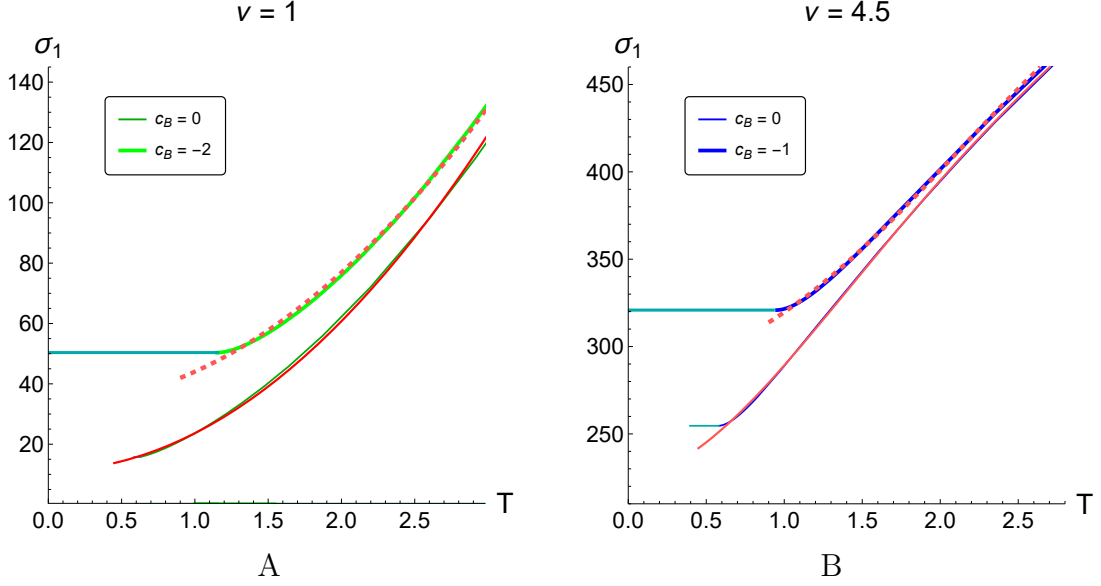


Figure 21. Spatial string tension σ_1 in the first orientation \mathcal{W}_{xY_1} as a function of temperature T at $\mu = 0$ for (A) isotropic case $\nu = 1$ that the solid red curve is $11.2 + 12.4 T^2$, the dashed red curve is $33.1 + 10.9 T^2$, and for (B) anisotropic case $\nu = 4.5$, the solid red curve is $226.1 + 91.3 T^2 - 31.9 T^3 + 3.7 T^4$ and the dashed red curve is $288.2 + 31.9 T^2 + 0.8 T^3 - 1.4 T^4$; $[\sigma]^{\frac{1}{2}} = [T] = [\mu] = [c_B]^{\frac{1}{2}} = \text{GeV}$.

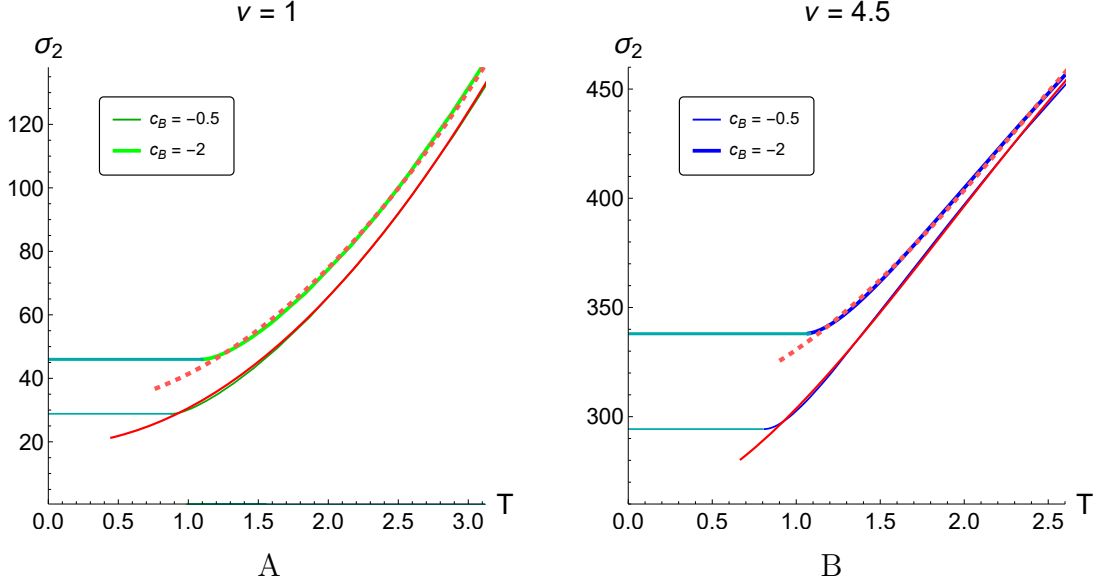


Figure 22. Spatial string tension σ_2 in the second orientation \mathcal{W}_{xY_2} as a function of temperature T at $\mu = 0$ for (A) isotropic case $\nu = 1$ that the solid red curve is $18.9 + 11.7 T^2$, the dashed red curve is $30.2 + 11.1 T^2$, and for (B) anisotropic case $\nu = 4.5$ the solid red curve is $258.3 + 58.1 T^2 - 13.6 T^3 + 0.9 T^4$, and the dashed red curve is $303.6 + 26.7 T^2 + 1.3 T^3 - 1.1 T^4$; $[\sigma]^{\frac{1}{2}} = [T] = [\mu] = [c_B]^{\frac{1}{2}} = \text{GeV}$.

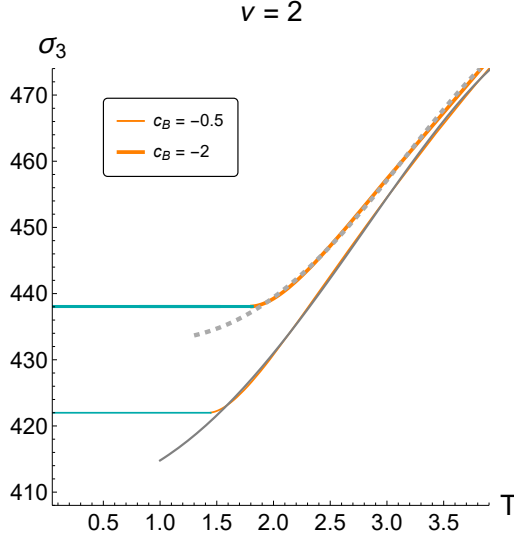


Figure 23. Spatial string tension σ_3 in the third orientation $\mathcal{W}_{y_1 y_2}$ as a function of temperature T at $\mu = 0$ for anisotropic case $\nu = 2$ the solid gray curve is $409.6 + 4.5 T^2 + 0.9 T^3 - 0.3 T^4$, and the dashed gray curve is $433.8 - 4.3 T^2 + 3.9 T^3 - 0.6 T^4$; $[\sigma]^{\frac{1}{2}} = [T] = [\mu] = [c_B]^{\frac{1}{2}} = \text{GeV}$.

tion, i.e. the drag force. Our results reveal, that for $T < T_{cr}$ the string tension value is temperature independent and gets a constant value. Similar behavior is reported in [85] and also in lattice calculations [86, 87]. In our model for all orientations at $T < T_{cr}$ the string tension profile is realized on the DW configuration and at $T > T_{cr}$ it is realized on the horizon configuration and it increases monotonically.

6 Conclusion

In this paper, we investigate the effective potential and the spatial string tension σ and its phase transitions between the DW configuration and the horizon configuration using spatial Wilson loops. To do this, we used the Einstein-dilaton-three-Maxwell action and incorporated a 5-dimensional metric with a special warp factor to construct an anisotropic holographic model under a strong magnetic field for the heavy-quark case [45]. In addition, the effect of spatial anisotropy ν , that reflects the noncentrality of HIC, on the string tension for three particular orientations is studied.

We obtained the SWL and the effective potential for general orientations, namely the dependence of σ on temperature T is studied for three particular SWL orientations, i.e. σ_i , $i = 1, 2, 3$ corresponding to \mathcal{W}_{xY_1} , \mathcal{W}_{xY_2} , and $\mathcal{W}_{y_1Y_2}$, respectively.

Let us summarize our findings, depending on different orientations.

- *The first SWL orientation \mathcal{W}_{xY_1} :*
 - some similarities between the zero-boundary condition (2.10) and the physical-boundary condition (2.12):
 - * the phase diagram and the DW coordinates do not depend on the boundary condition,
 - * inclusion of spatial anisotropy $\nu = 4.5$ decreases the values of the critical transition T between the DW and the horizon configuration in our model;
 - the main difference between the zero- and physical-boundary conditions:
 - * inclusion of spatial anisotropy $\nu = 4.5$ and increasing the magnetic field c_B causes the spatial string tension σ_1 to increase/decrease at zero/physical-boundary conditions,
 - * at very low T in the case of $\mu = 0$ with $c_B \neq 0$, the σ_1 exists/does not exist at zero/physical-boundary conditions due to the absence of the DW coordinate.
- *The second SWL orientation \mathcal{W}_{xY_2} :*
 - the spatial string tension σ increases with the spatial anisotropy ν and the external magnetic field c_B ;

- the transition temperature occurs at lower values in the second SWL orientation, \mathcal{W}_{xY_2} , compared to the first orientation, \mathcal{W}_{xY_1} , for both the isotropic case $\nu = 1$ and the anisotropic case $\nu = 4.5$.
- *The third SWL orientation $\mathcal{W}_{y_1Y_2}$:*
 - for $\nu = 1$ the effective potential values and the DW coordinates are exactly the same as the results for the second SWL orientation \mathcal{W}_{xY_2} , see (3.19) and (3.20);
 - for $\nu = 4.5$ there are no DW coordinates; in fact, there is a critical value of anisotropy $\nu_{cr} = 2.5$, i.e. at $\nu \geq 2.5$ the DW coordinates disappear;
 - for $\nu = 2$ the transition temperature has higher values in the third SWL orientation, $\mathcal{W}_{y_1Y_2}$, compared to the first \mathcal{W}_{xY_1} and second orientations \mathcal{W}_{xY_2} for all values of the magnetic field c_B .

There also are some properties, that are common and independent of the different SWL orientations choice, which are summarized as follows.

Universal characteristics

- The phase transition has magnetic catalysis behavior, which means that the critical temperature T_{cr} increases as the magnetic field c_B increases.
- As the magnetic field c_B increases, the value of the DW coordinate decreases, meaning the phase transition occurs at a smaller holographic coordinate z closer to the boundary.
- DW coordinates are independent of the chemical potential value.
- At lower temperature $T < T_{cr}$ in the DW configuration the string tension is independent of the temperature.
- At higher temperature $T > T_{cr}$ in the horizon configuration the string tension increases monotonically.
- Inclusion of the external magnetic field and spatial anisotropy enhance the string tension in the horizon configuration, i.e. the drag force.
- For the fully isotropic case $\nu = 1$ and $c_B = 0$ the temperature dependence of the string tension $\sigma \propto T^2$ is qualitatively consistent with the lattice results [86, 87].

It is very interesting to compare the phase transition between the DW and the horizon configuration, obtained by SWL, with the confinement/deconfinement phase transition line, obtained from temporal WL and the 1st-order phase transition line following from the thermodynamics of the model. Fig. 24 shows this comparison for different values of magnetic field $c_B = 0, -0.005, -0.05, -0.5 \text{ GeV}^2$, and different spatial anisotropies $\nu = 1, 1.5, 3, 4.5$. In this comparison the 2nd orientation of SWL, xY_2 , is used, while for temporal WL, tY_2 orientation is considered. The phase transition line obtained by SWL is depicted by a red dashed line, the confinement/deconfinement phase transition is depicted by a blue dashed line, and the first-order phase transition is depicted by a solid magenta line. The blue regions represent the QGP phase, the green regions correspond to the quarkyonic phase, and the brown regions correspond to the confined phase.

Fig. 24 depicts, that at small μ and for spatially isotropic case $\nu = 1$ the transition temperature via SWL is lower than the confinement/deconfinement transition temperature and higher than the 1st order phase transition temperature. However, including anisotropies $\nu = 1.5$, $\nu = 3$, and $\nu = 4.5$, our result shows that for any μ the transition temperature via SWL is always higher than the confinement/deconfinement and the 1st order transition temperature.

Note that diffusion coefficient is studied near the critical point in terms of temperature [70], and also temperature dependence of diffusion coefficient is investigated in [88] near the phase transition in isotropic backgrounds. Studying and extending the diffusion coefficient in the anisotropic background that we introduced in this research will be considered for future research.

Furthermore, it would be interesting to take into account other anisotropic models with different warp factors $b_s(z)$, corresponding to the light quark model [18] or the heavy quark model [40], to study the DW coordinates and string tension. Recently, this background has been used in holographic QCD to investigate the jet quenching parameter [82].

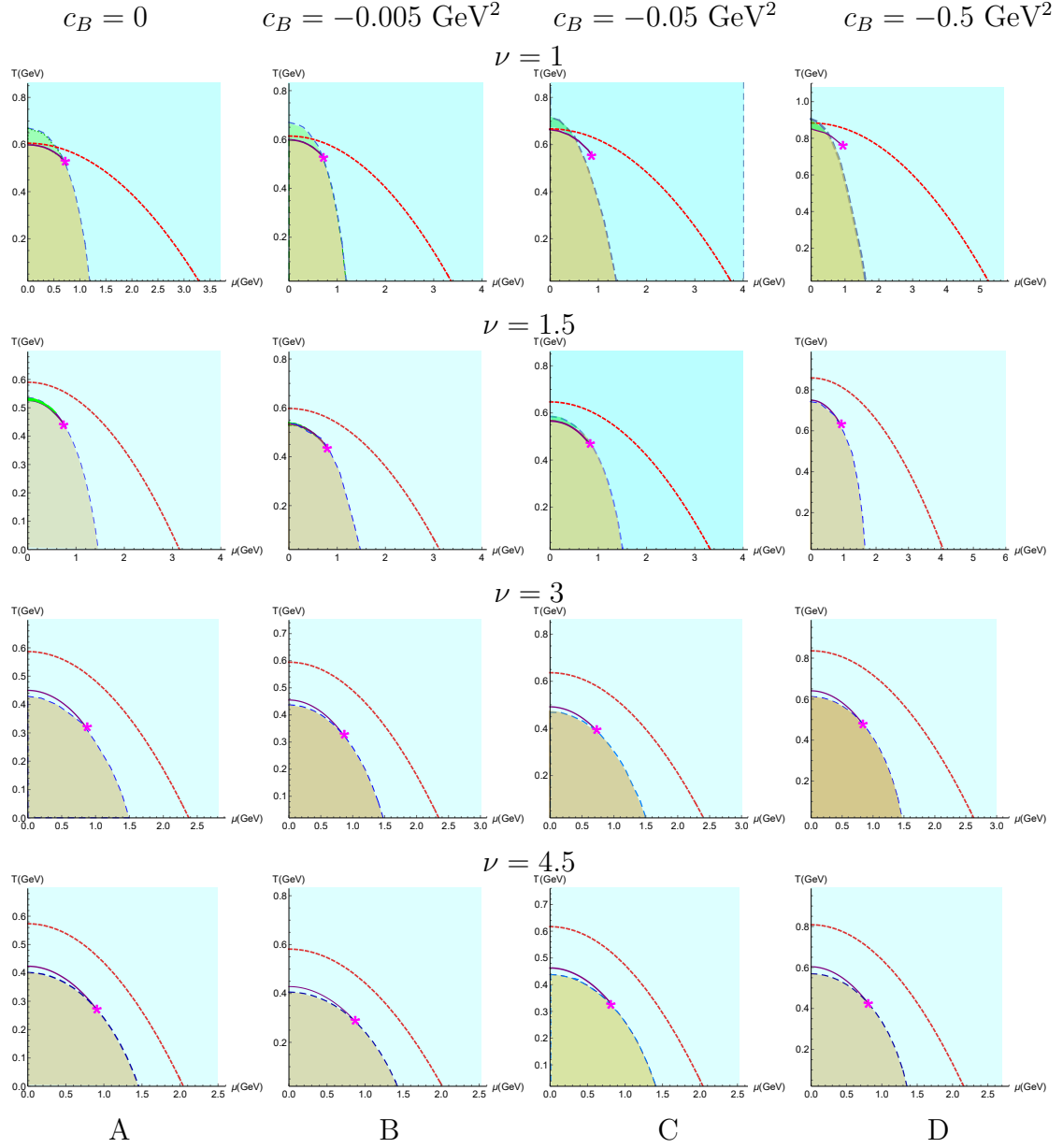


Figure 24. Phase diagrams in (μ, T) -plane for HQ models in columns (A) $c_B = 0$, (B) $c_B = -0.005 \text{ GeV}^2$, (C) $c_B = -0.05 \text{ GeV}^2$, and (D) $c_B = -0.5 \text{ GeV}^2$. The first, second, third, and forth raw shows $\nu = 1$, $\nu = 1.5$, $\nu = 3$, and $\nu = 4.5$, respectively.

Acknowledgments

The work of I.A. and P.S. was performed at the Steklov International Mathematical Center and supported by the Ministry of Science and Higher Education of the Russian Federation (agreement no. 075-15-2025-303). The work of A. H. was started at the Steklov International Mathematical Center and supported by the Ministry of Science and Higher Education of the Russian Federation (Agreement No. 075-15-2022-265). The work of I. A. and P. S. is also supported by Theoretical Physics and Mathematics Advancement Foundation “BASIS (grant No. 24-1-1-82-1, grant No. 23-1-4-43-1, respectively).

Appendix

A Solution of EOMs

Varying Lagrangian (2.1) over the metric we get the Einstein equations of motion (EOMs):

$$G_{\mu\nu} = T_{\mu\nu}, \quad (\text{A.1})$$

where

$$G_{\mu\nu} = R_{\mu\nu} - \frac{1}{2}g_{\mu\nu}R, \quad \frac{\delta S_m}{\delta g^{\mu\nu}} = T_{\mu\nu}\sqrt{-g}, \quad (\text{A.2})$$

and varying Lagrangian over the fields we get field equations

$$D_\mu D^\mu \phi + V'(\phi) + \sum_{i=0,1,3} \frac{f'_i(\phi)}{4} F_{(i)}^2 = 0, \quad (\text{A.3})$$

$$\partial_\mu (\sqrt{-g} f_i F_{(i)}^{\mu\nu}) = 0. \quad (\text{A.4})$$

The explicit forms of EOMs are given by

$$A''_t + A'_t \left(\frac{\mathfrak{b}'}{2\mathfrak{b}} + \frac{f'_0}{f_0} + \frac{\nu-2}{\nu z} + c_B z \right) = 0, \quad (\text{A.5})$$

$$g'' + g' \left(\frac{3\mathfrak{b}'}{2\mathfrak{b}} - \frac{\nu+2}{\nu z} + c_B z \right) - \left(\frac{z}{L} \right)^2 \frac{f_0 (A'_t)^2}{\mathfrak{b}} - \left(\frac{z}{L} \right)^{\frac{2}{\nu}} \frac{q_3^2 f_3}{\mathfrak{b}} = 0, \quad (\text{A.6})$$

$$\mathfrak{b}'' - \frac{3(\mathfrak{b}')^2}{2\mathfrak{b}} + \frac{2\mathfrak{b}'}{z} - \frac{4\mathfrak{b}}{3\nu z^2} \left(1 - \frac{1}{\nu} + \left(1 - \frac{3\nu}{2} \right) c_B z^2 - \frac{\nu c_B^2 z^4}{2} \right) + \frac{\mathfrak{b} (\phi')^2}{3} = 0, \quad (\text{A.7})$$

$$2g' \left(1 - \frac{1}{\nu} \right) + 3g \left(1 - \frac{1}{\nu} \right) \left(\frac{\mathfrak{b}'}{\mathfrak{b}} - \frac{4(\nu+1)}{3\nu z} + \frac{2c_B z}{3} \right) + \left(\frac{L}{z} \right)^{1-\frac{4}{\nu}} \frac{L e^{-c_B z^2} q_1^2 f_1}{\mathfrak{b}} = 0, \quad (\text{A.8})$$

$$2g' \left(1 - \frac{1}{\nu} + c_B z^2 \right) + 3g \left[\left(1 - \frac{1}{\nu} + c_B z^2 \right) \left(\frac{\mathfrak{b}'}{\mathfrak{b}} - \frac{4}{3\nu z} + \frac{2c_B z}{3} \right) - \frac{4(\nu-1)}{3\nu z} \right] + \\ + \left(\frac{L}{z} \right)^{1-\frac{4}{\nu}} \frac{L e^{-c_B z^2} q_1^2 f_1}{\mathfrak{b}} - \left(\frac{z}{L} \right)^{1+\frac{2}{\nu}} \frac{L q_3^2 f_3}{\mathfrak{b}} = 0, \quad (\text{A.9})$$

$$\frac{\mathfrak{b}''}{\mathfrak{b}} + \frac{(\mathfrak{b}')^2}{2\mathfrak{b}^2} + \frac{3\mathfrak{b}'}{\mathfrak{b}} \left(\frac{g'}{2g} - \frac{\nu+1}{\nu z} + \frac{2c_B z}{3} \right) - \frac{g'}{3zg} \left(5 + \frac{4}{\nu} - 3c_B z^2 \right) + \\ + \frac{8}{3z^2} \left(1 + \frac{3}{2\nu} + \frac{1}{2\nu^2} \right) - \frac{4c_B}{3} \left(1 + \frac{3}{2\nu} - \frac{c_B z^2}{2} \right) + \frac{g''}{3g} + \frac{2}{3} \left(\frac{L}{z} \right)^2 \frac{\mathfrak{b}V}{g} = 0. \quad (\text{A.10})$$

For more details, we refer the interested reader to [45].

B Arbitrary orientations of Wilson loop

In the holographic approach, the Nambu-Goto action in the background (3.5) for the probe string is

$$S = \frac{1}{2\pi\alpha'} \int d\xi^1 d\xi^2 \sqrt{-\det h_{\alpha\beta}}, \quad (\text{B.1})$$

where the induced metric $h_{\alpha\beta}$ is given by

$$h_{\alpha\beta} = G_{\mu\nu} \partial_\alpha X^\mu \partial_\beta X^\nu \quad (\text{B.2})$$

and is the orientation dependent. Here we use the same orientation to parametrize the rectangular Wilson loop as was considered to calculate the entanglement entropy using the rectangular parallelepiped in [81].

To parameterize the world-sheet of string, we use the rotation matrix $M(\phi, \theta, \psi)$ in a 3-dimensional space with the representation

$$x^i = \sum_{j=1,2,3} a_{ij}(\phi, \theta, \psi) \zeta^j, \quad i = 1, 2, 3, \quad (\text{B.3})$$

where a_{ij} in terms of the Euler angles ϕ, θ, ψ are the components of the rotation matrix

$$M(\phi, \theta, \psi) = \begin{pmatrix} a_{11}(\phi, \theta, \psi) & a_{12}(\phi, \theta, \psi) & a_{13}(\phi, \theta, \psi) \\ a_{21}(\phi, \theta, \psi) & a_{22}(\phi, \theta, \psi) & a_{23}(\phi, \theta, \psi) \\ a_{31}(\phi, \theta, \psi) & a_{32}(\phi, \theta, \psi) & a_{33}(\phi, \theta, \psi) \end{pmatrix}, \quad (\text{B.4})$$

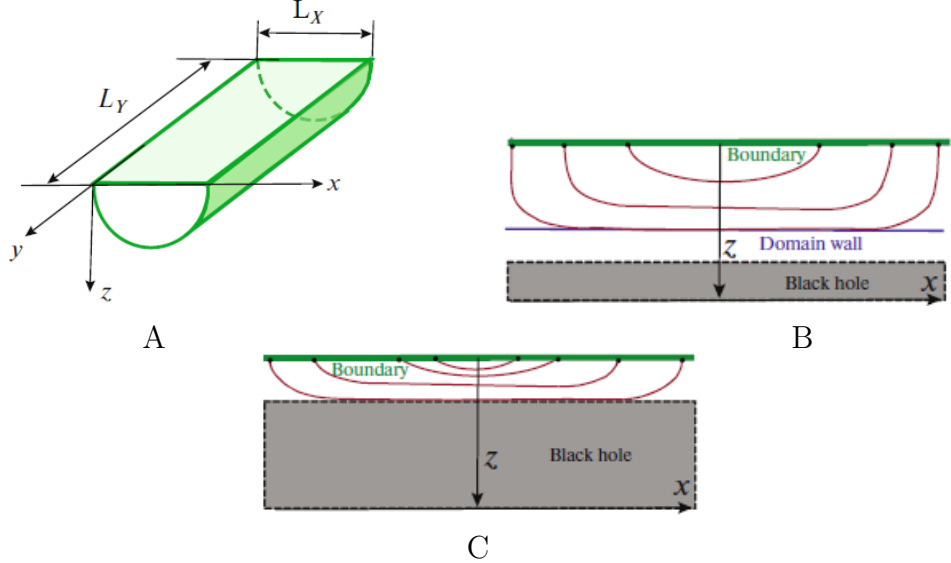


Figure 25. (A) Spatial Wilson loop and its world-sheet. (B) Describing the DW configuration and the horizon configuration. (C) After the phase transition from DW configuration to horizon configuration [6]; $[T] = [\mu] = \text{GeV}$.

where

$$\begin{aligned}
 a_{11}(\phi, \theta, \psi) &= \cos \phi \cos \psi - \cos \theta \sin \phi \sin \psi, \\
 a_{12}(\phi, \theta, \psi) &= -\cos \psi \sin \phi - \cos \phi \cos \theta \sin \psi, \\
 a_{13}(\phi, \theta, \psi) &= \sin \theta \sin \psi, \\
 a_{21}(\phi, \theta, \psi) &= \cos \theta \cos \psi \sin \phi + \cos \phi \sin \psi, \\
 a_{22}(\phi, \theta, \psi) &= \cos \phi \cos \theta \cos \psi - \sin \phi \sin \psi, \\
 a_{23}(\phi, \theta, \psi) &= -\cos \psi \sin \theta, \\
 a_{31}(\phi, \theta, \psi) &= \sin \phi \sin \theta, \\
 a_{32}(\phi, \theta, \psi) &= \cos \phi \sin \theta, \\
 a_{33}(\phi, \theta, \psi) &= \cos \theta.
 \end{aligned} \tag{B.5}$$

Here ϕ is the angle between the ζ^1 -axis and the node line (N), θ is the angle between the ζ^3 and x^3 -axes, and ψ is the angle between the node line N and x^1 -axis; see Fig. 26.

We use the following embedding to describe the 2-dimensional world-sheet of string in the 5-dimensional bulk:

$$\begin{aligned}
 X^0(\xi) &= \text{const}, \\
 X^i(\xi) &= \sum_{\alpha=1,2} a_{i\alpha}(\phi, \theta, \psi) \xi^\alpha, \quad i = 1, 2, 3, \quad \alpha = 1, 2, \\
 X^4(\xi) &= z(\xi^1),
 \end{aligned} \tag{B.6}$$

where X^i are spatial coordinates.

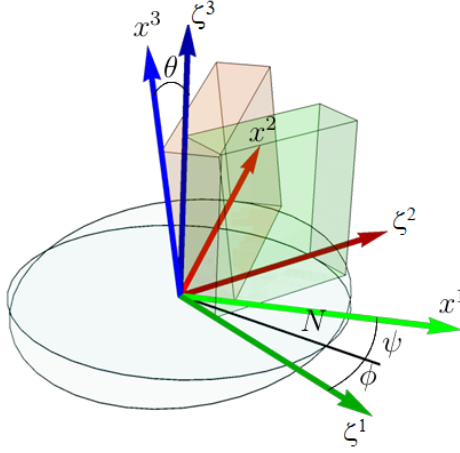


Figure 26. Rotating the green rectangular cube by the Euler angles (ϕ, θ, ψ) , we get the pink cube oriented along the axes (x^1, x^2, x^3) . The node line is denoted by N , and $(\zeta^1, \zeta^2, \zeta^3)$ are axes before rotation [81].

The line element of the induced metric on the world-sheet is

$$ds_{ws}^2 = g_{\alpha\beta} d\xi^\alpha d\xi^\beta, \quad \alpha, \beta = 1, 2. \quad (\text{B.7})$$

After applying the embedding relations (B.6) the induced metric can be written as

$$\begin{aligned} ds_{ws}^2 &= \frac{L^2 \mathfrak{b}_s(z)}{z^2} \left(\sum_{i=1,2,3} \mathfrak{g}_i(z) d(x^i)^2 + \frac{d(x^4)^2}{g} \right) \\ &= \frac{L^2 \mathfrak{b}_s(z)}{z^2} \left(\sum_{i=1,2,3} \mathfrak{g}_i(z) \left(\sum_{j=1,2} a_{ij}(\phi, \theta, \psi) d\xi^j \right)^2 + z'^2 \frac{d(\xi^1)^2}{g(z)} \right). \end{aligned} \quad (\text{B.8})$$

We have

$$g_{\alpha\beta} = \frac{L^2 \mathfrak{b}_s(z)}{z^2} \bar{g}_{\alpha\beta}, \quad (\text{B.9})$$

$$\begin{aligned} \bar{g}_{11}(z, \phi, \theta, \psi) &= \mathfrak{g}_1 a_{11}^2 + \mathfrak{g}_2 a_{21}^2 + \mathfrak{g}_3 a_{31}^2 + \frac{z'^2}{g}, \\ \bar{g}_{22}(z, \phi, \theta, \psi) &= \mathfrak{g}_1 a_{12}^2 + \mathfrak{g}_2 a_{22}^2 + \mathfrak{g}_3 a_{32}^2, \\ \bar{g}_{12}(z, \phi, \theta, \psi) &= \mathfrak{g}_1 a_{11} a_{12} + \mathfrak{g}_2 a_{21} a_{22} + \mathfrak{g}_3 a_{31} a_{32}, \\ \bar{g}_{21} &= \bar{g}_{12}. \end{aligned} \quad (\text{B.10})$$

The determinant of the induced metric is given by

$$\begin{aligned} \det g_{\alpha\beta} &= \left(\frac{L^2 \mathfrak{b}_s}{z^2} \right)^2 \left(\left(\mathfrak{g}_1 a_{11}^2 + \mathfrak{g}_2 a_{21}^2 + \mathfrak{g}_3 a_{31}^2 + \frac{z'^2}{g} \right) (\mathfrak{g}_1 a_{12}^2 + \mathfrak{g}_2 a_{22}^2 + \mathfrak{g}_3 a_{32}^2) - \right. \\ &\quad \left. - (\mathfrak{g}_1 a_{11} a_{12} + \mathfrak{g}_2 a_{21} a_{22} + \mathfrak{g}_3 a_{31} a_{32})^2 \right). \end{aligned} \quad (\text{B.11})$$

The Nambu-Goto action for SWL is given by

$$\mathcal{S}_{SWL} = \frac{1}{2\pi\alpha'} \int_{\mathcal{W}} \left(\frac{L^2 \mathfrak{b}_s}{z^2} \right) \sqrt{\left(\mathfrak{g}_1 \mathfrak{g}_2 a_{33}^2 + \mathfrak{g}_1 \mathfrak{g}_3 a_{23}^2 + \mathfrak{g}_2 \mathfrak{g}_3 a_{13}^2 + \frac{z'^2}{g} \bar{g}_{22} \right)} d\xi^1 d\xi^2, \quad (\text{B.12})$$

where the integration is over the world-sheet \mathcal{W} components and g , \mathfrak{g}_1 , \mathfrak{g}_2 , \mathfrak{g}_3 are functions of z and \bar{g}_{22} , \bar{g}_{33} , \bar{g}_{23} are functions of z and Euler angles. The effective potential can be obtained as

$$\mathcal{V}(z(\xi)) = \frac{1}{2\pi\alpha'} \left(\frac{L^2 \mathfrak{b}_s}{z^2} \right) \sqrt{\mathfrak{g}_1 \mathfrak{g}_2 a_{33}^2 + \mathfrak{g}_1 \mathfrak{g}_3 a_{23}^2 + \mathfrak{g}_2 \mathfrak{g}_3 a_{13}^2}. \quad (\text{B.13})$$

Note that the action (B.12) and the effective potential (B.13) depend on the angles of rotation and anisotropy.

C String tension at DW and horizon configurations

Using equation (3.2), the first integral related to the action (3.1) is given by

$$\frac{M(z(\xi)) \mathcal{F}(z(\xi))}{\sqrt{\mathcal{F}(z(\xi)) + (z'(\xi))^2}} = \mathcal{I}. \quad (\text{C.1})$$

At the turning point $z = z_*$, where the minimal surface has the closest distance to the horizon, we have $z'(\xi) = 0$. Then, from (C.1) one can obtain

$$M(z_*) \sqrt{\mathcal{F}(z_*)} = \mathcal{I}. \quad (\text{C.2})$$

Utilizing (C.1) and (C.2) to find z' , the length ℓ and the action \mathcal{S} (3.1) are given by general formulas

$$\frac{\ell}{2} = \int_{\epsilon}^{z_*} \frac{1}{\sqrt{\mathcal{F}(z)}} \frac{dz}{\sqrt{\frac{\mathcal{V}^2(z)}{\mathcal{V}^2(z_*)} - 1}}, \quad (\text{C.3})$$

$$\frac{\mathcal{S}}{2} = \int_{\epsilon}^{z_*} \frac{M(z) dz}{\sqrt{1 - \frac{\mathcal{V}^2(z_*)}{\mathcal{V}^2(z)}}}, \quad (\text{C.4})$$

where ϵ is the regulator in gravity theory and corresponds to the UV cut-off in gauge theory. Taking into account the limit $\ell \rightarrow \infty$, we have two categories.

- There is a stationary point of $\mathcal{V}(z)$ that

$$\mathcal{V}' \Big|_{z_{DW}} = 0, \quad (\text{C.5})$$

where $z = z_{DW}$ is a DW coordinate that can be considered equal to the turning point $z_* = z_{DW}$. Near the turning point we have

$$\sqrt{\frac{\mathcal{V}^2(z)}{\mathcal{V}^2(z_{DW})} - 1} = \sqrt{\frac{\mathcal{V}''(z_{DW})}{\mathcal{V}'(z_{DW})}} (z - z_*) + \mathcal{O}((z - z_*)^2). \quad (\text{C.6})$$

The using (C.3) and (C.4) one gets

$$\ell \underset{z \rightarrow z_*}{\sim} \frac{1}{\sqrt{\mathcal{F}(z_{DW})}} \sqrt{\frac{\mathcal{V}(z_{DW})}{\mathcal{V}''(z_{DW})}} \log(z - z_*), \quad (\text{C.7})$$

$$\mathcal{S} \underset{z \rightarrow z_*}{\sim} M(z_{DW}) \sqrt{\frac{\mathcal{V}(z_{DW})}{\mathcal{V}''(z_{DW})}} \log(z - z_*). \quad (\text{C.8})$$

Therefore

$$\mathcal{S} \sim M(z_{DW}) \sqrt{\mathcal{F}(z_{DW})} \ell. \quad (\text{C.9})$$

Then we have

$$\sigma_{DW} = M(z_{DW}) \sqrt{\mathcal{F}(z_{DW})}, \quad (\text{C.10})$$

where σ_{DW} is the spatial string tension in the DW configuration.

- There is no stationary point in the region $0 < z < z_h$ for $\mathcal{V}(z)$. We suppose the near horizon expansion

$$\mathcal{F}(z) = \mathfrak{F}(z_h)(z - z_h) + \mathcal{O}((z - z_h)^2). \quad (\text{C.11})$$

In this configuration, the string stretches on the horizon and we take $z_* = z_h$. We propose two items:

- if $M(z_h) \neq \infty$, we have

$$\ell \rightarrow \infty, \quad (\text{C.12})$$

$$S \rightarrow 0; \quad (\text{C.13})$$

- if $M(z) \underset{z \rightarrow z_h}{\rightarrow} \infty$ as

$$M(z) \underset{z \sim z_h}{\sim} \frac{\mathfrak{m}(z_h)}{\sqrt{z - z_h}}; \quad (\text{C.14})$$

then, using (C.3) and (C.4) we have

$$\ell \underset{z \rightarrow z_h}{\sim} \frac{1}{\sqrt{\mathfrak{F}(z_h)}} \frac{1}{\sqrt{\frac{2\mathcal{V}'(z_h)}{\mathcal{V}(z_h)}}} \log(z - z_h), \quad (\text{C.15})$$

$$\mathcal{S} \underset{z \rightarrow z_h}{\sim} \mathfrak{m}(z_h) \frac{1}{\sqrt{\frac{2\mathcal{V}'(z_h)}{\mathcal{V}(z_h)}}} \log(z - z_h), \quad (\text{C.16})$$

and therefore

$$\sigma_{z_h} = \mathfrak{m}(z_h) \sqrt{\mathfrak{F}(z_h)}, \quad (\text{C.17})$$

where σ_{z_h} is the spatial string tension in the horizon configuration.

References

- [1] J. Casalderrey-Solana, H. Liu, D. Mateos, K. Rajagopal and U. Achim Wiedemann, “Gauge/String Duality, Hot QCD and Heavy Ion Collisions”, Cambridge University Press, 2014, ISBN 978-1-009-40350-4, 978-1-009-40349-8, 978-1-009-40352-8, 978-1-139-13674-7 [arXiv:1101.0618 [hep-th]].
- [2] I. Y. Aref’eva, “Holographic approach to quark–gluon plasma in heavy ion collisions”, *Phys. Usp.* **57**, 527-555 (2014).
- [3] O. DeWolfe, S. S. Gubser, C. Rosen and D. Teaney, “Heavy ions and string theory,” *Prog. Part. Nucl. Phys.* **75**, 86-132 (2014) [arXiv:1304.7794 [hep-th]].
- [4] I. Aref’eva, “Holography for Heavy-Ion Collisions at LHC and NICA. Results of the last two years”, *EPJ Web Conf.* **191**, 05010 (2018)
- [5] I. Aref’eva, “Holography for Heavy Ions Collisions at LHC and NICA”, *EPJ Web Conf.* **164**, 01014 (2017) [arXiv:1612.08928 [hep-th]]
- [6] I. Aref’eva, “Holography for Nonperturbative Study of QFT”, *Phys. Part. Nucl.* **51**, no.4, 489-496 (2020).
- [7] R. G. Cai, S. He and D. Li, “A hQCD model and its phase diagram in Einstein-Maxwell-Dilaton system”, *JHEP* **03**, 033 (2012) [arXiv:1201.0820 [hep-th]].
- [8] S. He, S. Y. Wu, Y. Yang and P. H. Yuan, “Phase Structure in a Dynamical Soft-Wall Holographic QCD Model”, *JHEP* **04**, 093 (2013) [arXiv:1301.0385 [hep-th]].
- [9] Y. Yang and P. H. Yuan, “A Refined Holographic QCD Model and QCD Phase Structure”, *JHEP* **11**, 149 (2014) [arXiv:1406.1865 [hep-th]].
- [10] Y. Yang and P. H. Yuan, “Confinement-deconfinement phase transition for heavy quarks in a soft wall holographic QCD model”, *JHEP* **12**, 161 (2015) [arXiv:1506.05930 [hep-th]].
- [11] Z. Fang, S. He and D. Li, “Chiral and Deconfining Phase Transitions from Holographic QCD Study”, *Nucl. Phys. B* **907**, 187-207 (2016) [arXiv:1512.04062 [hep-ph]].
- [12] K. Chelabi, Z. Fang, M. Huang, D. Li and Y. L. Wu, “Chiral Phase Transition in the Soft-Wall Model of AdS/QCD”, *JHEP* **04**, 036 (2016) [arXiv:1512.06493 [hep-ph]].
- [13] D. Li and M. Huang, “Chiral phase transition of QCD with $N_f = 2 + 1$ flavors from holography”, *JHEP* **02**, 042 (2017) [arXiv:1610.09814 [hep-ph]].
- [14] I. Aref’eva and K. Rannu, “Holographic Anisotropic Background with Confinement-Deconfinement Phase Transition”, *JHEP* **05**, 206 (2018) [arXiv:1802.05652 [hep-th]].
- [15] Z. Fang, Y. L. Wu and L. Zhang, “Chiral phase transition and QCD phase diagram from AdS/QCD”, *Phys. Rev. D* **99**, no.3, 034028 (2019) [arXiv:1810.12525 [hep-ph]].

- [16] I. Aref'eva, K. Rannu and P. Slepov, “Orientation Dependence of Confinement-Deconfinement Phase Transition in Anisotropic Media”, *Phys. Lett. B* **792**, 470-475 (2019) [arXiv:1808.05596 [hep-th]].
- [17] J. Chen, S. He, M. Huang and D. Li, “Critical exponents of finite temperature chiral phase transition in soft-wall AdS/QCD models”, *JHEP* **01**, 165 (2019) [arXiv:1810.07019 [hep-ph]].
- [18] I. Y. Aref'eva, K. Rannu and P. Slepov, “Holographic anisotropic model for light quarks with confinement-deconfinement phase transition”, *JHEP* **06**, 090 (2021) [arXiv:2009.05562 [hep-th]].
- [19] F. R. Brown, F. P. Butler, H. Chen, N. H. Christ, Z. h. Dong, W. Schaffer, L. I. Unger and A. Vaccarino, “On the existence of a phase transition for QCD with three light quarks”, *Phys. Rev. Lett.* **65**, 2491-2494 (1990)
- [20] O. Philipsen, “Constraining the phase diagram of QCD at finite temperature and density”, *PoS LATTICE2019*, 273 (2019) [arXiv:1912.04827 [hep-lat]].
- [21] O. Andreev and V. I. Zakharov, “On Heavy-Quark Free Energies, Entropies, Polyakov Loop, and AdS/QCD”, *JHEP* **04**, 100 (2007) [arXiv:hep-ph/0611304 [hep-ph]].
- [22] U. Gursoy, E. Kiritsis, L. Mazzanti and F. Nitti, “Holography and Thermodynamics of 5D Dilaton-gravity”, *JHEP* **05**, 033 (2009) [arXiv:0812.0792 [hep-th]].
- [23] U. Gursoy, E. Kiritsis, L. Mazzanti and F. Nitti, “Improved Holographic Yang-Mills at Finite Temperature: Comparison with Data”, *Nucl. Phys. B* **820**, 148-177 (2009) [arXiv:0903.2859 [hep-th]].
- [24] S. He, M. Huang and Q. S. Yan, “Logarithmic correction in the deformed AdS_5 model to produce the heavy quark potential and QCD beta function”, *Phys. Rev. D* **83**, 045034 (2011) [arXiv:1004.1880 [hep-ph]].
- [25] U. Gursoy, E. Kiritsis, L. Mazzanti, G. Michalogiorgakis and F. Nitti, “Improved Holographic QCD”, *Lect. Notes Phys.* **828**, 79-146 (2011) [arXiv:1006.5461 [hep-th]].
- [26] P. Colangelo, F. Giannuzzi, S. Nicotri and V. Tangorra, “Temperature and quark density effects on the chiral condensate: An AdS/QCD study”, *Eur. Phys. J. C* **72**, 2096 (2012) [arXiv:1112.4402 [hep-ph]].
- [27] D. Li, M. Huang and Q. S. Yan, “A dynamical soft-wall holographic QCD model for chiral symmetry breaking and linear confinement”, *Eur. Phys. J. C* **73**, 2615 (2013) [arXiv:1206.2824 [hep-th]].
- [28] D. Li and M. Huang, “Dynamical holographic QCD model for glueball and light meson spectra”, *JHEP* **11**, 088 (2013) [arXiv:1303.6929 [hep-ph]].
- [29] D. Li, S. He and M. Huang, “Temperature dependent transport coefficients in a dynamical holographic QCD model”, *JHEP* **06**, 046 (2015) [arXiv:1411.5332 [hep-ph]].

[30] K. Chelabi, Z. Fang, M. Huang, D. Li and Y. L. Wu, “Realization of chiral symmetry breaking and restoration in holographic QCD”, *Phys. Rev. D* **93**, no.10, 101901 (2016) [arXiv:1511.02721 [hep-ph]].

[31] M. W. Li, Y. Yang and P. H. Yuan, “Approaching Confinement Structure for Light Quarks in a Holographic Soft Wall QCD Model”, *Phys. Rev. D* **96**, no.6, 066013 (2017) [arXiv:1703.09184 [hep-th]].

[32] I. Y. Aref’eva, A. A. Golubtsova and G. Policastro, “Exact holographic RG flows and the $A_1 \times A_1$ Toda chain”, *JHEP* **05**, 117 (2019) [arXiv:1803.06764 [hep-th]].

[33] X. Chen, D. Li, D. Hou and M. Huang, “Quarkyonic phase from quenched dynamical holographic QCD model”, *JHEP* **03**, 073 (2020) [arXiv:1908.02000 [hep-ph]].

[34] M. W. Li, Y. Yang and P. H. Yuan, “Analytic Study on Chiral Phase Transition in Holographic QCD”, *JHEP* **02**, 055 (2021) [arXiv:2009.05694 [hep-th]].

[35] D. Giataganas, “Probing strongly coupled anisotropic plasma”, *JHEP* **07**, 031 (2012) [arXiv:1202.4436 [hep-th]].

[36] D. Giataganas and H. Soltanpanahi, “Heavy Quark Diffusion in Strongly Coupled Anisotropic Plasmas”, *JHEP* **06**, 047 (2014) [arXiv:1312.7474 [hep-th]].

[37] D. Giataganas, U. Gürsoy and J. F. Pedraza, “Strongly-coupled anisotropic gauge theories and holography”, *Phys. Rev. Lett.* **121**, no.12, 121601 (2018) [arXiv:1708.05691 [hep-th]].

[38] K. Bitaghsir Fadafan and R. Morad, “Jets in a strongly coupled anisotropic plasma,” *Eur. Phys. J. C* **78** (2018) no.1, 16 [arXiv:1710.06417 [hep-th]].

[39] H. Bohra, D. Dудal, A. Hajilou and S. Mahapatra, “Anisotropic string tensions and inversely magnetic catalyzed deconfinement from a dynamical AdS/QCD model”, *Phys. Lett. B* **801**, 135184 (2020) [arXiv:1907.01852 [hep-th]].

[40] H. Bohra, D. Dудal, A. Hajilou and S. Mahapatra, “Chiral transition in the probe approximation from an Einstein-Maxwell-dilaton gravity model”, *Phys. Rev. D* **103**, no.8, 086021 (2021) [arXiv:2010.04578 [hep-th]].

[41] S. I. Finazzo, R. Critelli, R. Rougemont and J. Noronha, “Momentum transport in strongly coupled anisotropic plasmas in the presence of strong magnetic fields”, *Phys. Rev. D* **94**, no.5, 054020 (2016) [erratum: *Phys. Rev. D* **96**, no.1, 019903 (2017)] [arXiv:1605.06061 [hep-ph]].

[42] I. Aref’eva, K. Rannu and P. Slepov, “Cornell potential for anisotropic QGP with non-zero chemical potential”, *EPJ Web Conf.* **222**, 03023 (2019)

[43] M. Asadi and A. Hajilou, “Meson potential energy in a non-conformal holographic model”, *Nucl. Phys. B* **979**, 115744 (2022) [arXiv:2112.04209 [hep-th]].

[44] E. Brehm, “Heavy Quarks in Strongly Coupled Non-Conformal Plasmas with Anisotropy”, *JHEP* **06**, 128 (2019) [arXiv:1711.08943 [hep-th]].

[45] I. Y. Aref’eva, A. Hajilou, K. Rannu and P. Slepov, “Magnetic catalysis in

holographic model with two types of anisotropy for heavy quarks”, Eur. Phys. J. C **83**, no.12, 1143 (2023) [arXiv:2305.06345 [hep-th]].

[46] I. Y. Aref’eva, A. Ermakov, K. Rannu and P. Slepov, “Holographic model for light quarks in anisotropic hot dense QGP with external magnetic field”, Eur. Phys. J. C **83**, no.1, 79 (2023) [arXiv:2203.12539 [hep-th]].

[47] I. Y. Aref’eva, K. Rannu and P. Slepov, “Holographic model for heavy quarks in anisotropic hot dense QGP with external magnetic field”, JHEP **07**, 161 (2021) [arXiv:2011.07023 [hep-th]].

[48] I. Y. Aref’eva, K. Rannu and P. Slepov, “Energy Loss in Holographic Anisotropic Model for Heavy Quarks in External Magnetic Field,” [arXiv:2012.05758 [hep-th]].

[49] I. Y. Aref’eva and A. A. Golubtsova, “Shock waves in Lifshitz-like spacetimes”, JHEP **04**, 011 (2015) [arXiv:1410.4595 [hep-th]].

[50] J. Adam *et al.* [ALICE], “Centrality Dependence of the Charged-Particle Multiplicity Density at Midrapidity in Pb-Pb Collisions at $\sqrt{s_{\text{NN}}} = 5.02$ TeV”, Phys. Rev. Lett. **116**, no.22, 222302 (2016) [arXiv:1512.06104 [nucl-ex]].

[51] V. Skokov, A. Y. Illarionov and V. Toneev, “Estimate of the magnetic field strength in heavy-ion collisions”, Int. J. Mod. Phys. A **24**, 5925-5932 (2009) [arXiv:0907.1396 [nucl-th]].

[52] A. Bzdak and V. Skokov, “Event-by-event fluctuations of magnetic and electric fields in heavy ion collisions”, Phys. Lett. B **710**, 171-174 (2012) [arXiv:1111.1949 [hep-ph]].

[53] W. T. Deng and X. G. Huang, “Event-by-event generation of electromagnetic fields in heavy-ion collisions”, Phys. Rev. C **85**, 044907 (2012) [arXiv:1201.5108 [nucl-th]].

[54] A. Deur, S. J. Brodsky and C. D. Roberts, “QCD running couplings and effective charges”, Prog. Part. Nucl. Phys. **134**, 104081 (2024) [arXiv:2303.00723 [hep-ph]].

[55] I. Y. Aref’eva, A. Hajilou, A. Nikolaev and P. Slepov, “Holographic QCD running coupling for light quarks in strong magnetic field”, Phys. Rev. D **110**, no.8, 8 (2024) [arXiv:2407.11924 [hep-th]].

[56] I. Y. Aref’eva, A. Hajilou, A. Nikolaev and P. Slepov, “Holographic QCD Running Coupling for Heavy Quarks in Strong Magnetic Field”, [arXiv:2503.07521 [hep-th]].

[57] R. Rougemont, R. Critelli and J. Noronha, “Holographic calculation of the QCD crossover temperature in a magnetic field”, Phys. Rev. D **93**, no.4, 045013 (2016) [arXiv:1505.07894 [hep-th]].

[58] D. Li, M. Huang, Y. Yang and P. H. Yuan, “Inverse Magnetic Catalysis in the Soft-Wall Model of AdS/QCD”, JHEP **02**, 030 (2017) [arXiv:1610.04618 [hep-th]].

[59] U. Gursoy, M. Jarvinen and G. Nijs, “Holographic QCD in the Veneziano Limit at a Finite Magnetic Field and Chemical Potential”, Phys. Rev. Lett. **120**, no.24, 242002 (2018) [arXiv:1707.00872 [hep-th]].

[60] U. Gürsoy, M. Järvinen, G. Nijs and J. F. Pedraza, “On the interplay between magnetic field and anisotropy in holographic QCD”, *JHEP* **03**, 180 (2021) [arXiv:2011.09474 [hep-th]].

[61] L. Shahkarami, “Magnetized Einstein–Maxwell-dilaton model under an external electric field”, *Eur. Phys. J. C* **82**, no.1, 33 (2022) [arXiv:2111.04813 [hep-th]].

[62] P. Slepov, “Magnetic versus inverse magnetic catalysis in hot and dense quark matter,” *Int. J. Mod. Phys. A* **39** (2024) no.35, 2443015

[63] S. S. Jena, J. Barman, B. Toniato, D. Dudal and S. Mahapatra, “A dynamical Einstein-Born-Infeld-dilaton model and holographic quarkonium melting in a magnetic field”, *JHEP* **12**, 096 (2024) [arXiv:2408.14813 [hep-th]].

[64] D. S. Ageev, I. Y. Aref’eva, A. A. Golubtsova and E. Gourgoulhon, “Thermalization of holographic Wilson loops in spacetimes with spatial anisotropy”, *Nucl. Phys. B* **931**, 506-536 (2018) [arXiv:1606.03995 [hep-th]].

[65] A. A. Golubtsova and V. H. Nguyen, “Wilson Loops in Exact Holographic RG Flows at Zero and Finite Temperatures”, *Theor. Math. Phys.* **202**, no.2, 214-230 (2020) [arXiv:1906.12316 [hep-th]].

[66] C. P. Herzog, A. Karch, P. Kovtun, C. Kozcaz and L. G. Yaffe, “Energy loss of a heavy quark moving through $N=4$ supersymmetric Yang-Mills plasma”, *JHEP* **07**, 013 (2006) [arXiv:hep-th/0605158 [hep-th]].

[67] S. S. Gubser, “Drag force in AdS/CFT”, *Phys. Rev. D* **74**, 126005 (2006) [arXiv:hep-th/0605182 [hep-th]].

[68] J. Casalderrey-Solana and D. Teaney, “Heavy quark diffusion in strongly coupled $N=4$ Yang-Mills”, *Phys. Rev. D* **74**, 085012 (2006) [arXiv:hep-ph/0605199 [hep-ph]].

[69] S. J. Sin and I. Zahed, “Ampere’s Law and Energy Loss in AdS/CFT Duality”, *Phys. Lett. B* **648**, 318-322 (2007) [arXiv:hep-ph/0606049 [hep-ph]].

[70] O. Andreev, “Drag Force on Heavy Quarks and Spatial String Tension”, *Mod. Phys. Lett. A* **33**, no.06, 1850041 (2018) [arXiv:1707.05045 [hep-ph]].

[71] S. S. Gubser, “Comparing the drag force on heavy quarks in $N=4$ super-Yang-Mills theory and QCD”, *Phys. Rev. D* **76**, 126003 (2007) [arXiv:hep-th/0611272 [hep-th]].

[72] U. Gursoy, E. Kiritsis, G. Michalogiorgakis and F. Nitti, “Thermal Transport and Drag Force in Improved Holographic QCD”, *JHEP* **12**, 056 (2009) [arXiv:0906.1890 [hep-ph]].

[73] K. B. Fadafan and H. Soltanpanahi, “Energy loss in a strongly coupled anisotropic plasma,” *JHEP* **10** (2012), 085 [arXiv:1206.2271 [hep-th]].

[74] M. Chernicoff, D. Fernandez, D. Mateos and D. Trancanelli, “Drag force in a strongly coupled anisotropic plasma”, *JHEP* **08**, 100 (2012) [arXiv:1202.3696 [hep-th]].

[75] R. Rougemont, A. Ficnar, S. Finazzo and J. Noronha, “Energy loss, equilibration,

and thermodynamics of a baryon rich strongly coupled quark-gluon plasma”, JHEP **04**, 102 (2016) [arXiv:1507.06556 [hep-th]].

[76] Z. R. Zhu, S. Q. Feng, Y. F. Shi and Y. Zhong, “Energy loss of heavy and light quarks in holographic magnetized background”, Phys. Rev. D **99**, no.12, 126001 (2019) [arXiv:1901.09304 [hep-ph]].

[77] I. Y. Aref’eva, A. Hajilou, P. Slepov and M. Usova, “Running coupling for holographic QCD with heavy and light quarks: Isotropic case”, Phys. Rev. D **110**, no.12, 126009 (2024) [arXiv:2402.14512 [hep-th]].

[78] I. Y. Aref’eva, A. Hajilou, P. Slepov and M. Usova, “Beta-functions and RG flows for holographic QCD with heavy and light quarks: Isotropic case”, Phys. Rev. D **111**, no.4, 046013 (2025) [arXiv:2503.09444 [hep-th]].

[79] I. Y. Aref’eva, A. Hajilou, P. Slepov and M. Usova, “Beta-function dependence on the running coupling in holographic QCD models”, Teor. Mat. Fiz. **221**, no.3, 2132-2143 (2024) [arXiv:2407.14448 [hep-th]].

[80] P. S. Slepov, “A Way To Improve the String Tension Dependence on Temperature in Holographic Model”, Phys. Part. Nucl. **52** (2021) no.4, 560-563

[81] I. Y. Aref’eva, A. Patrushev and P. Slepov, “Holographic entanglement entropy in anisotropic background with confinement-deconfinement phase transition”, JHEP **07**, 043 (2020) [arXiv:2003.05847 [hep-th]].

[82] I. Y. Aref’eva, A. Hajilou, A. Nikolaev and P. Slepov, “Jet quenching in holographic QCD as an indicator of phase transitions in anisotropic regimes,” Phys. Rev. D **112**, no.12, 126007 (2025) [arXiv:2507.19426 [hep-th]].

[83] P. Slepov, “Jet Quenching in Anisotropic Holographic QCD: Probing Phase Transitions and Critical Regions,” Moscow Univ. Phys. Bull. (2025) [arXiv:2512.24204 [hep-th]].

[84] O. Andreev and V. I. Zakharov, “Heavy-quark potentials and AdS/QCD”, Phys. Rev. D **74**, 025023 (2006) [arXiv:hep-ph/0604204 [hep-ph]].

[85] O. Andreev and V. I. Zakharov, “The Spatial String Tension, Thermal Phase Transition, and AdS/QCD”, Phys. Lett. B **645**, 437-441 (2007) [arXiv:hep-ph/0607026 [hep-ph]].

[86] D. Bala, O. Kaczmarek, P. Petreczky, S. Sharma and S. Tah, “Spatial String Tension and Its Effects on Screening Correlators in a Thermal QCD Plasma”, Phys. Rev. Lett. **135**, no.1, 012301 (2025) [arXiv:2501.17943 [hep-lat]].

[87] Y. Maezawa *et al.* [WHOT-QCD], “Heavy-quark free energy, debye mass, and spatial string tension at finite temperature in two flavor lattice QCD with Wilson quark action”, Phys. Rev. D **75**, 074501 (2007) [arXiv:hep-lat/0702004 [hep-lat]].

[88] Z. R. Zhu, J. X. Chen, X. M. Liu and D. Hou, “Thermodynamics and energy loss in D dimensions from holographic QCD model”, Eur. Phys. J. C **82**, no.6, 560 (2022) [arXiv:2109.02366 [hep-ph]].